UNIVERSITY OF HELSINKI REPORT SERIES IN PHYSICS

Atomistic simulations of room temperature plasticity in amorphous oxide materials

Jiahui Zhang

Helsinki Accelerator Laboratory
Division of Materials Physics
Department of Physics
Faculty of Science
University of Helsinki
Helsinki, Finland

DOCTORAL DISSERTATION

To be presentedfor public discussion with the permission of the Faculty of Science of University of Helsinki, in Hall 129, Chemicum Building, on the 8th of July, 2024 at 13 o'clock.

HELSINKI 2024

Supervising professor

Professor — Flyura Djurabekova
University of Helsinki, Department of Physics
Helsinki Institute of Physics

Supervisors

Senior University Lecturer — Antti Kuronen
University of Helsinki, Department of Physics

Doctor — Erkka J. Frankberg
Tampere University, Materials Science and Environmental Engineering Unit

Pre-examiners

Professor — Matti Alatalo
University of Oulu

Professor — Adam Foster
Aalto University

Opponent

Professor — Morten Mattrup Smedskjær
Aalborg University,
Department of Chemistry and Bioscience

ISBN 978-952-84-0154-4 (printed version)
ISSN 0356-0961
Helsinki 2024
Unigrafia Oy

ISBN 978-952-84-0155-1 (PDF version)
ISSN 2954-3142
`https://ethesis.helsinki.fi`
Helsinki 2024
Electronic Publications @ University of Helsinki
(Helsingin yliopiston verkkojulkaisut)

Jiahui Zhang, **Atomistic simulations of room temperature plasticity in amorphous oxide materials, University of Helsinki, 2024, 73 p. + appendices, University of Helsinki Report Series in Physics, ISBN 978-952-84-0154-4, ISSN 0356-0961 (Printed version), ISBN 978-952-84-0155-1, ISSN 2954-3142 (PDF version)**

Abstract

From the windows of a structure to the display of a mobile device, amorphous materials play a crucial role in various aspects of our daily lives. The indispensable characteristics of amorphous materials, such as transparency to visible light, insulation, and resistance to oxidation, are heavily relied upon by individuals. However, the extensive utilization of amorphous materials is constrained by their inadequate mechanical performance. The lack of a proficient plastic deformation mechanism renders amorphous materials incapable of withstanding significant strain, often leading to severe fractures.

Recently, experimental findings have shown that thin films of amorphous aluminum oxide (a-Al_2O_3) exhibit noticeable plasticity at room temperature during mechanical testing. Unlike traditional amorphous materials, the preparation of a-Al_2O_3 requires specific procedures, primarily through gas phase deposition. This distinction in preparation methods contributes to structural differences between a-Al_2O_3 and other amorphous oxide materials, potentially resulting in varying abilities for plastic deformation.

The molecular dynamics method is a potent approach for investigating the mechanical characteristics of materials at a microscopic level. In this study, it is employed to explore the plastic deformation mechanism of amorphous aluminum oxide, along with various characterization methods that primarily target the medium-range order (MRO). Our main finding is that during the process of stretching or compressing amorphous aluminum oxide, the dominant mechanism that averts material failure is viscous flow.

In order to broaden our understanding, we have devised a coarse-grained analytical approach that concentrates on scales larger than atomic, specifically targeting medium-range structural characteristics. Through this model, we found that the plasticity of a material might be impacted by the structural features at the coarse-grained level. This approach is applicable to both simple or complex amorphous oxides (single or multiple cation types), offering a quantitative assessment of their ability to undergo plastic deformation.

Contents

Abstract v
Contents vi
Common abbreviations ix
List of symbols x

1 Introduction **1**

2 Purpose and structure **3**
2.1 Summaries of publications 3
2.2 Author's contribution 6

3 Room temperature plasticity in amorphous materials **7**
3.1 Oxide glasses 8
3.2 Glass transition 8
3.2.1 Angell plot 9
3.2.2 Kauzmann paradox 9
3.2.3 Glass transition temperature 10
3.3 Plastic deformation 11
3.3.1 Brittle fracture 11
3.3.2 Plastic deformation in crystalline materials 12
3.3.3 Plastic deformation in amorphous materials 12
3.4 Experimental observations of nano-scale plasticity in amorphous alumina 13

4 Methods **17**

4.1 Molecular dynamics methods 17

4.1.1 Classical molecular dynamics 17

4.1.2 Interatomic potentials 20

4.1.3 Modeling the quenching process and mechanical tests with molecular dynamics simulation 23

4.2 Structural analysis methods 24

5 Atomistic simulation of room temperature plasticity of oxide glass materials **29**

5.1 Dependence of glass transition temperature on cooling rate 29

5.2 Plastic deforming mechanism in amorphous alumina 35

5.3 Understanding the plastic deformation mechanism from a coarse-grained level 39

5.4 Plastic behavior of amorphous gallium oxide 44

6 Summary and Outlook **53**

Acknowledgements 55

References 57

Common abbreviations

SRO Short-range ordering

MRO Medium-range ordering

LRO Long-range ordering

FEM Finite element method

MD Molecular dynamics

DFT Density functional theory

AIMD *ab initio* molecular dynamics

RDF Radial distribution function

BAD Bond angle distribution

ML Machine-learning

IAP Interatomic potential

LPSE Localized plastic strain event

PNCE Polyhedral neighbor change event

ESph Edge-sharing polyhedron

CSph Corner-sharing polyhedron

List of symbols

k_{B}	Boltzmann's constant
q	Cooling rate
η	Viscosity
τ	Relaxation time
m	Fragility
E	Young's modulus
$\mathbf{T}_{\mathrm{g}}$	Glass transition temperature
$\mathrm{D}^2_{\mathrm{min}}$	Non-affine squared displacement
ρ	Density
ε	Strain
ε_{max}	Maximum strain
ε_{flow}	Flow strain
σ	Stress
σ_{max}	Maximum stress
σ_{flow}	Flow stress

Chapter 1

Introduction

A substantial part of the materials on Earth are believed to be amorphous, but what we know about this special state of the material is still quite limited. For example, the history of using glass, which is also amorphous, can be as long as the oldest human civilization, but it is still not completely clear about what is the key factor that makes the material a glass former. The amorphous material affects all aspects of modern life, and the weakness of this material, brittleness, has been commonly known and carried by people since the beginning of using this material. Researchers have put great effort into finding stronger amorphous materials and keeping their unique functionalities at the same time, but the findings are limited.

It has been widely acknowledged that the amorphous materials are brittle because of the lack of an effective plastic deformation mechanism. When mechanical tests are performed, the stress tends to concentrate at the weak points of the structure, leading to catastrophic failure of the material. Recently, Frankberg *et al.* [1, 2] found that amorphous aluminum oxide could endure considerable compressive and tensile stress without fracture. This enlightens the investigation of novel amorphous materials. They proposed that the key prerequisite for plasticity is that the structure be free of flaws. So, stress will not quickly concentrate around them. However, the microscopic mechanism behind plastic deformation is unclear.

Several challenges limit the experimental investigation of amorphous materials. The first limit is the preparation process. Although conventional amorphous materials can be easily prepared, some novel amorphous materials usually have higher preparation requirements. Metallic glasses need a high enough cooling rate to be prepared, whereas alumina requires a cooling rate far faster to be prepared amorphous, as estimated. Another limit is the characterization methods. Because of the absence of long-range order, methods that can be used in characterizing crystals are not as effective for amorphous materials. The stochastic atomic environment of amorphous materials makes extracting useful information

especially challenging. A proper characterization method can significantly boost the research of amorphous materials.

Computational methods, such as atomistic simulation, are a powerful tool in the field of material science. The nanoscale structure of the material is a focus and provides valuable and reliable data from a microscopic perspective. Furthermore, the cooling or heating rates, which are believed to be very hard to achieve experimentally, can be easily achieved using the molecular dynamics method. Therefore, a large amount of literature has implemented atomistic simulation methods in the field of material science. With the advantages mentioned above, in this work, the molecular dynamics method is applied to investigate the plastic deformation mechanism in amorphous materials. To deepen our understanding of this material, a new coarse-grained characterization method is developed. With these tools, the plastic deformation mechanism is thoroughly investigated, and the knowledge is extended to a more general scale of oxide amorphous materials.

Chapter 2

Purpose and structure

The purpose of this thesis is to contribute to the understanding of the plastic deformation mechanism of amorphous oxide materials with the help of molecular dynamics methods. A considerable part of the thesis focused on the development of quantitative characterization methods to allow a more comprehensive comparison between materials.

The thesis is structured as follows. In the following, we first list and summarize the publications included in this article-based thesis, and briefly describe the author's contribution to each article. In Chapter 3, we briefly introduce the knowledge about amorphous materials, glass transition, and plastic deformation. Chapter 4 includes the simulation and characterization methods used in this thesis. In Chapter 5, we present the results of the computational investigation of plastic deformation in oxide amorphous materials. The summary and outlook are given in Chapter 6.

2.1 Summaries of publications

Publication I: Dependence between glass transition and plasticity in amorphous aluminum oxide: a molecular dynamics study
J. Zhang, M. De Meulder, E. Frankberg and A. Kuronen
Journal of Non-Crystalline Solids, **628**, 122840 (2024)

In this work, we investigated the glass transition of amorphous aluminum oxide and verified the existence of the glass transition during cooling of the material. We characterized the structure in multiple ways and attempted to reveal medium-range structural information about the structure. When studying the influence of the cooling rate on plastic behavior, we found that it is essential to focus on the medium-range ordering of the structure because it produces more evident differences in the structures prepared with different cooling rates. The results of the tensile test also show that the mechanical work input could work similarly to the thermal energy input. Structural memory is erased during the tensile test, and consequently an identical structure is reached.

Publication II: Exceptional Microscale Plasticity in Amorphous aluminum Oxide at Room Temperature
E. Frankberg, A. Lambai, J. Zhang, J. Kalikka, S. Khakalo, B. Paladino, M. Cabrioli, N. Mathews, T. Salminen, M. Hokka, J. Akola, A. Kuronen, E. Levänen, F. Di Fonzo and G. Mohanty
Advanced Materials, **35**, 2303142 (2023)

We conducted a combined experimental and modeling study of the plastic deformation mechanism of amorphous aluminum oxide. On the experimental side, compression tests are performed on the micropillars of amorphous aluminum oxide. The results show that as the strain rate increased, the predominant plastic deformation mechanism switched from homogeneous plastic flow to shear banding. On the atomistic simulation side, we observed the formation of localized plastic flow during compression simulations, which indicates a viscous flow-mediated plastic deformation mechanism. Furthermore, we noticed that, at lower strain rates, the localized plastic flow emerges homogeneously in the system. At higher strain rates, there tend to be fewer but larger localized plastic flows, forming close to the 45-degree shear band.

Publication III: Room Temperature Plasticity in a-silica and a-alumina: a Computational and Topological study
J. Zhang, E. Frankberg, J. Kalikka and A. Kuronen
Acta Materialia, **259**, 119223 (2023)

In this work, we studied the brittle-to-ductile transition in amorphous silica and compared the plastic deformation ability of amorphous aluminum oxide and densified silica. We proposed a coarse-grained analysis model that can be applied to a more general field of amorphous oxides. When this model was applied to amorphous alumina and silica, we quantitatively investigated the plastic deformation ability of these two materials. From normal amorphous silica to densified silica, we noticed that the increase in edge-sharing polyhedra fraction could be one of the factors leading to better plastic deformation ability. On the basis of the characterization results, we conclude that the high fraction of edge-sharing polyhedra structure could be the reason why amorphous alumina has extraordinary plastic deformation ability.

Publication IV : Large-scale Atomistic Study of Plasticity in Amorphous Gallium Oxide with a Machine-learning Potential
J. Zhang, J. Zhao, J. Byggmästar, E. Frankberg, and A. Kuronen
To be published

Gallium is in the same group as aluminum. The oxygens of these two elements are believed to have many similarities because the cation-oxygen bond formed by these two elements is similar. On the basis of a newly developed machine learning interatomic potential, we investigated the mechanical properties of gallium oxide, including the plastic deformation ability with large-scale atomistic simulations. The results verified that the mechanical properties of gallium oxide are highly similar to those of amorphous alumina. We also predict that amorphous gallium oxide also has an extraordinary plastic deformation ability. However, with proper characterization methods, we still capture differences in the plastic deformation ability between these two materials, again validating the importance of characterizing the medium-range structural information.

2.2 Author's contribution

The author was the first author, conducted part of the molecular dynamics simulation and analysis, and partly wrote and modified the manuscript of Publication I. The author is the major contributor to the computational part of Publication II and participated in the creation and modification of the manuscript. The author was the first author, conducted all the molecular dynamics simulations, and created and modified the manuscript of Publication III. The author was the first author, conducted all molecular dynamics simulations, created, and modified the manuscript of Publication IV.

Chapter 3

Room temperature plasticity in amorphous materials

Amorphous materials are generally considered with present short-range ordering (SRO) and absent long-range ordering. They are widely used in industry fields, providing valuable functional properties [3–9]. As the usage of amorphous materials becomes wider, a deeper understanding of them becomes increasingly vital. The definition of the amorphous state is not as clear as that of crystalline phases because they are not a form with obvious phase transition processes and clearly defined lattice structures. Amorphous materials are defined from the perspective of their structure. If a material exhibits SRO in the solid state but lacks LRO, *i.e.*, it loses periodicity at a sufficiently long distance, it is called an amorphous material. Glasses are the most commonly known amorphous materials that have a long history of use [10, 11]. They are generally prepared from inorganic minerals through high-temperature melting and cooling processes. Usually, if an amorphous material exhibits a glass transition when prepared in a melt-quench process, then it is glass. Therefore, glass material is a term included in amorphous materials that also includes many materials such as oxide glasses, metallic glasses, and organic polymers.

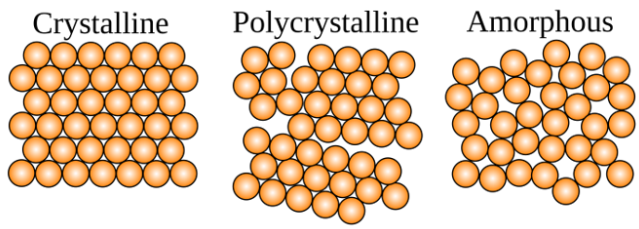


Figure 3.1: Illustration of different atom arrangements. Figure obtained from Wikipedia [12].

3.1 Oxide glasses

Oxide glasses have a historical background of usage that can be compared to the oldest human civilization. It has been widely recognized that glass could be produced using a melt-quench technique. For some commonly used glass formers like silicon oxide, allowing the melt to cool naturally would result in the formation of glass. Amorphous silica is a frequently utilized glass material in our everyday lives. Research on its structural [13–15] and mechanical properties [16–23] through experimental and computational studies began a long time ago. Despite being brittle at room temperature, studies using computer simulations have shown the potential for inducing a transition from brittle to ductile in amorphous silica [24–26], the mechanism of which remains unclear. It has been observed to exhibit remarkable nanoductility under specific conditions [27–30] such as at high pressures [31, 32], rapid cooling rates [33], or high strain rates [34].

However, there are also poor glass formers such as aluminum oxide and gallium oxide, which are believed to require an extremely fast cooling rate to achieve an amorphous state. aluminum oxide is a crucial material studied in this research and will have its characteristics and preparation requirements discussed later. Gallium belongs to the same group as aluminum and its oxide exhibits analogous phases with alumina and they are often investigated together and compared with each other [35–38]. Therefore, it is assumed that they share similar mechanical properties, including plastic deformation capability. Furthermore, gallium oxide is a semiconductor material with an exceptionally high band gap, significant critical electric field, low effective electron mass, and transparency [39–42].

In addition to oxide glasses, metallic glasses are also referred to as amorphous alloys. To produce metallic glass, rapid cooling rates of around 10^5 to 10^6 Ks^{-1} are required to prevent crystallization of the liquid alloy [43–45]. Experimental evidence of the disordered atomic structure of metallic glass strongly aligns with Zachariasen's proposed atomic arrangement for glass materials almost a century ago [46–48]. Metallic glasses exhibit exceptional strength and toughness, even surpassing that of steel [49, 50]. Nonetheless, a drawback of metallic glasses is their limited ductility, leading to catastrophic failure upon fracture, similar to many other glass materials. The absence of a periodic atomic configuration in amorphous materials presents a difficulty in material characterization because the traditional methods used for crystalline materials, both computational and experimental, are no longer suitable.

3.2 Glass transition

The early knowledge was that relatively few materials could be made amorphous. However, as technology develops, it has been acknowledged that amorphization could occur in most materials, even water [51, 52]. When the liquid is cooled

at a cooling rate that is high enough, crystallization can be avoided even below the melting temperature. Instead, the motion of the atoms becomes slower, and the viscosity of the liquid increases. As the liquid gets colder, the atoms would finally be unable to adjust their positions and appear as if they were "frozen" in the liquid-like configuration.

3.2.1 Angell plot

For materials such as silica and germanium oxide, the dependence of viscosity η on temperature exhibits an Arrhenius behavior, given as

$$\eta = A \exp(\frac{E}{k_{\mathrm{B}}\mathrm{T}}), \tag{3.1}$$

where A and E represent temperature-independent constants, k_{B} denotes Boltzmann's constant, and T stands for temperature. However, some materials exhibit a departure from the Arrhenius law in terms of viscosity as they cool down. These materials experience a significant increase in viscosity when approaching the glass transition temperature, displaying super-Arrhenius behavior. As a result, Angell introduced the concept of classifying glass-forming materials into "strong" and "fragile" glass formers based on how their viscosity changes with temperature in the liquid state [53], as depicted in the Angell plot (Figure 3.2). Fragility (m) of a glass former can be quantitatively assessed by the rate of change of the natural logarithm of viscosity (η) at the glass transition temperature T_{g}:

$$m = \left.\frac{\partial \log \eta}{\partial(\mathrm{T_g}/\mathrm{T})}\right|_{T=T_g}. \tag{3.2}$$

Larger m indicates a more "fragile" glass former, and vice versa. A "strong" glass former adheres to the Arrhenius law during cooling from the liquid phase, whereas a "fragile" glass former demonstrates super-Arrhenius behavior. It is important to note that it is not completely clear whether this classification is correlated with the mechanical properties of the materials, although a possible connection between fragility and the Poisson ratio has been reported [54].

3.2.2 Kauzmann paradox

In addition to the noticeable variation in viscosity, the entropy of the liquid while it cools down also reveals intriguing findings. It is recognized that the entropy of a liquid surpasses that of its corresponding crystalline forms due to the higher heat capacity in the liquid compared to crystals. Upon cooling the liquid below its melting point, Kauzmann noted that an extrapolation of the entropy suggests that the entropy of the liquid would match that of the crystal at a temperature above zero. If this pattern persists, the entropy of the supercooled liquid will turn negative before the temperature reaches zero [56]. This apparent contradiction is

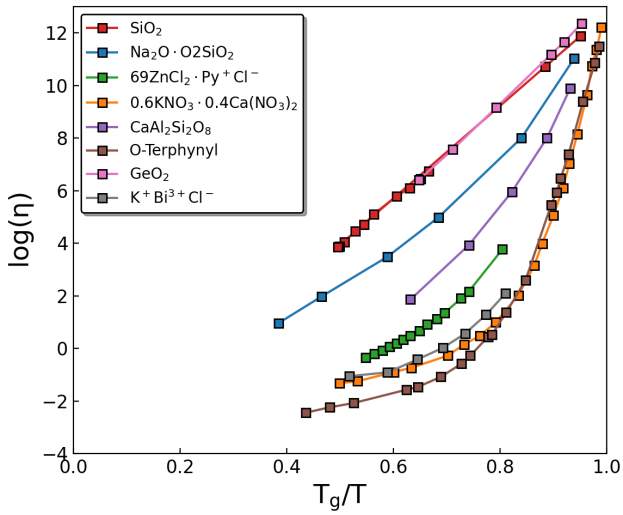


Figure 3.2: $T_g$scaled Arrhenius representation of liquid viscosities showing Angell's strong–fragile pattern. Strong liquids exhibit approximate linearity (Arrhenius behavior), indicative of a temperature-independent activation energy $E = dln\eta/d(1/T) \approx$ const. Fragile liquids exhibit super-Arrhenius behavior, their effective activation energy increasing as temperature decreases. Figure reprinted from Refs. [53] and [55].

commonly known as the "Kauzmann paradox". Nevertheless, the occurrence of a glass transition prevents this entropy dilemma. The liquid eventually transforms into a glassy state, and the relationship between entropy and temperature also shifts post the glass transition.

3.2.3 Glass transition temperature

Unlike crystallization, the appearance of a glass transition is usually accompanied by a continuous change in the properties of the material, such as potential energy and heat capacity [57]. This transition corresponds to a narrow temperature range named the glass transition temperature T_g. To clarify how T_g is determined, different definitions are proposed, below are some of the definitions:

1. The temperature at which the shear viscosity reaches 1×10^{13} poise when cooling the liquid;

2. The onset of the drastic increase in the heat capacity curve when heating the amorphous structure, which is also the onset of the ΔC_p peak [58, 59];

3. The intersection of the liquid and amorphous portions of the potential energy or density versus temperature curve's extrapolation (in atomistic simulations).

Based on *ab initio* calculations, T_g can be even possibly estimated from radial distribution functions [60]. At a reduced rate of cooling, the supercooled liquid would have a greater opportunity to explore its various configurations. Consequently, the atoms would have sufficient time to reach positions with lower energy levels before the viscosity reaches a point where atomic motion ceases entirely, resulting in a lower T_g. Conversely, faster cooling rates would yield a higher T_g as the atoms would have less time to reposition themselves rapidly [59]. This trend holds true when determining T_g through the heating process as well, a quicker heating rate would result in a higher glass transition temperature, while a slower rate would lead to a lower T_g.

3.3 Plastic deformation

3.3.1 Brittle fracture

Plastic deformation results from the permanent and irreversible relative displacement of large amounts of atoms in a material, which involves the breaking and re-combining of bonds compared to elastic displacement [61]. If the atoms do not recover to their original positions when the load is relieved from the structure, we can conclude that the deformation of the structure is plastic rather than elastic. An elastic deformation usually corresponds to a linear stress-strain correlation, but there also exist non-linear stress-strain correlations. Therefore, an offload test is required to distinguish whether the deformation is elastic or plastic. If the recombination of bonds occurs too late or too slowly after the breaking of bonds such that the strain has concentrated to fewer bonds left in the local region, a catastrophic breaking of bonds might happen. Then we see a fracture of the structure. This happens because fewer bonds need to hold the same amount of load, so each of them is holding a higher amount of load than before. The quantitative study of glass fracture was first conducted by Griffith in the 1920s [62]. The basic idea is that the elastic energy stored in the structure must exceed the surface energy of the two freshly formed fracture surfaces. The stored elastic energy can be formulated as

$$U = \frac{\pi \sigma^2 c^2}{E}, \tag{3.3}$$

where σ is the applied nominal stress, c is the crack size and E is Young's modulus. Assuming that no plastic deformation occurs during the strain, the elastic energy will fully contribute to the creation of the new fracture surfaces, thus the energy change would be

$$\Delta U = U - 4\gamma_s c, \tag{3.4}$$

where γ_s is the fracture surface energy. By differentiating the equation and equating it to zero we can reduce the equation to

$$\sigma_f \sqrt{\pi c_{\text{crit}}} = \sqrt{2E\gamma_s}, \tag{3.5}$$

where σ_f is the fracture stress and c_{crit} is the critical crack length above which the fracture would occur. The left-hand side is often named the "stress intensity factor" K_I, and the right-hand side is called the "critical stress intensity factor" K_{Ic}. However, experiments conducted with crystalline materials show a significant discrepancy between the measured values because of the existence of plastic deformation.

3.3.2 Plastic deformation in crystalline materials

Different mechanisms in crystals and amorphous materials dominate plastic deformation. In single crystals and metals, the most common source of plastic deformation is dislocation slip [63]. Because the energies required to break bonds are identical, the displacement of one atom can be quickly passed to the end of the dislocation or the surface, if there is no interaction with other dislocations. This explains why metals have extraordinary ductility because they have highly homogeneous lattice structures. In comparison, single-crystal ceramics have stronger covalent bonds and usually more than one element, making dislocation glide harder to occur. However, in polycrystals, not only interactions between dislocations but also interactions between grain boundaries and dislocations inhibit the dissipation of plastic deformation along the dislocations. Consequently, the plastic deformation ability is weaker for polycrystals compared to single crystals and metals and could exhibit different mechanisms [64].

Despite the limitation of charge equilibrium in an ionic system, diffusion-mediated plastic deformation mechanisms are also important in crystals and polycrystals. As a measurement of diffusion speed, it has been generally acknowledged that diffusion coefficients vary at different structures in polycrystals, as

$$D_{\text{l}} < D_{\text{p}} < D_{\text{gb}} < D_{\text{s}},$$

where D_{l} is the lattice diffusion coefficient, D_{p} is the pipe (dislocation line) diffusion coefficient, D_{gb} is the grain boundary diffusion coefficient, D_{s} is the surface diffusion coefficient. They can vary by several orders of magnitude, indicating different abilities in mediating plastic deformation. However, although diffusion along defects can be much faster than in the lattice, diffusion itself is a pretty slow mechanism. A typical phenomenon caused by this mechanism is the creep of both single-crystal and polycrystal aluminum oxide under pressure. When constant pressure is applied to a structure, researchers observed diffusion of vacancies from faces under tensile stress to faces under compressive stress [65].

3.3.3 Plastic deformation in amorphous materials

As the size of the grains decreases, the ordered structure over long distances gradually diminishes, eventually leading to the formation of an amorphous state,

which can be regarded as having atom-sized grains. Due to the absence of a conventional lattice structure in amorphous materials, defining defects becomes a challenging task. Consequently, structures such as dislocations and grain boundaries do not exist, giving rise to distinct plastic deformation mechanisms in amorphous materials compared to crystals. In such scenarios, each diffusion step requires varying amounts of energy, resulting in an exceptionally low diffusion coefficient in amorphous materials [2]. One well-known plastic deformation mechanism at elevated temperatures is viscous flow, commonly observed in the production of glass items. Viscous flow refers to the deformation of glass material under its own weight [66]. The viscosity of the glass material decreases as the temperature increases. At elevated temperatures, the behavior of the glass material is akin to that of a viscous Newtonian fluid when subjected to shear stress, where the deformation is accommodated through local stirring. Another mechanism present in the plastic deformation of amorphous materials is shear banding, often witnessed during the plastic deformation of metallic glasses. This phenomenon manifests as the localization of strain within bands approximately 10 nm wide, resembling the dislocation glide in metals or single crystals, but occurring in a broader region [67, 68].

Furthermore, it is challenging to prevent imperfections and voids in the industrial production of non-crystalline materials. These imperfections and voids may become weak points for strain accumulation when the material is subjected to stress. Consequently, non-crystalline materials are more prone to experiencing brittle fractures rather than plastic deformation. By managing imperfections in the manufacturing of non-crystalline materials, the occurrence of catastrophic fractures can be significantly reduced. Only then can the plastic properties of non-crystalline materials be thoroughly examined.

3.4 Experimental observations of nano-scale plasticity in amorphous alumina

aluminum oxide is a widely occurring ceramic material. Its most common crystalline phase is the α phase, also known as corundum, which has a Mohs hardness of 8, second only to diamond. Ceramic alumina has extraordinary heat resistance and can be prepared by sintering. It can also be used as a mediator component in the production of binary or multi-composition glass materials that have extraordinary mechanical properties and applications [69–71]. Although alumina is a widely existing functional glass, research on amorphous alumina is still limited compared to that on its single-crystal and polycrystalline states. The main reason is that it is prone to crystallization during the cooling process [72], or cracks may occur due to an uneven stress distribution when quenching from high temperatures. Despite the difficulties, using techniques such as the pulsed laser deposition technique (PLD) [73–75], amorphous alumina can be prepared. PLD

is performed in such a way that a high-energy laser is used to cause ablation on the surface of the target material, turning the atoms at the surface into a plasma plume. The plasma of charged ions would diffuse in the chamber and nucleate on the surface of the substrates. The cooling of the plasma is estimated to occur on the time scale of 100 ns [74], equivalent to a quenching rate of over 1×10^{10} Ks^{-1}. Such an extremely high quenching rate leads to the result that the prepared samples are usually amorphous.

Frankberg *et al.* successfully prepared thin films of amorphous alumina on sapphire and NaCl crystal substrates in their experiments [1]. Compression and tension experiments are performed in their work, and *in situ* characterization methods were used during the experiments. Samples with thicknesses of 60 nm on sapphire substrates were prepared for compressing tests. The compressive force is applied using a diamond indenter with a strain rate of 1 nm/s. Compression tests were performed with the beam on and off to investigate the effect of the electron beam. The stress-strain results show that after reaching a yield stress of 3.5 to 4.7 GPa, the samples continue to deform in a plastic way until an equivalent engineering strain of about 90 to 100%. After the yielding part, the stress stabilized in a narrow range and deformation occurred in a viscous creep fashion. For tensile test experiments, the amorphous thin film had a shape of 2 μm by 500 nm by 40 nm. In the tensile test, the fracture occurred with a mechanical strain of about 15%, but a permanent deformation was still observed after measuring the total length after the fracture. Researchers noted that fracture during the tensile test is possibly induced by flaws and voids formed during sample preparation. In both compression and tension experiments, the stress-strain curves showed clear plastic behavior of the material. After the linear increase in the elastic part, the sample started to yield and the curve stabilized at a stress called flow stress.

Based on the results of the TEM characterization of the compression experiments, Frankberg *et al.* proposed that viscous flow is probably the dominant mechanism behind the observed plastic behavior. Four reasons are proposed to support the conclusion. First, the samples are amorphous, which means that no dislocations would help the nucleation and movement of defects. Second, no clear necking is observed before deformation and fracture of the stretched sample. Third, the flow stress of the samples is nearly constant, which is expected if the material deforms by viscous flow. Fourth, the TEM characterization of the compressed samples proved the existence of surface diffusion.

In addition to the experimental study, the atomistic simulation method was also used. From a microscopic perspective, the simulation results gave possible sources of the exceptional plasticity in amorphous alumina compared to conventional glasses such as silica. They are the most active bond-switching ability, have the lower volume fraction of the cavities, and have a viscous flow during tension at room temperature. It gave insights from a microscopic perspective and showed promising potential for studying the room-temperature plasticity in amorphous

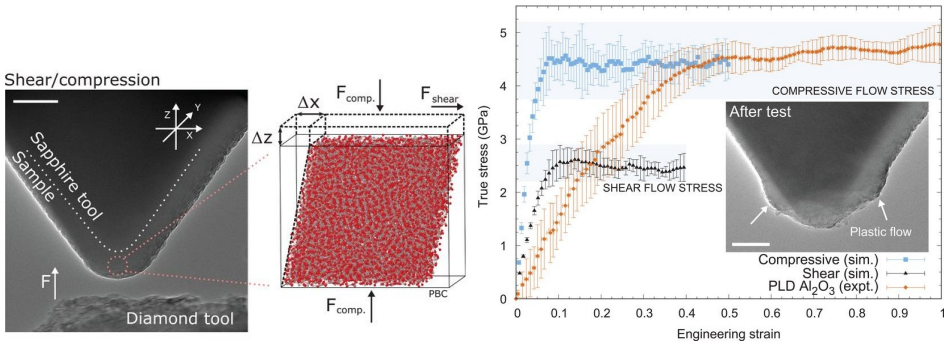


Figure 3.3: Experimental and simulation procedures to measure the viscous behavior of a-Al_2O_3 at ≈300 K. **(left)** In situ experimental shear compressive setup and simulation setups for separate shear and compression to measure permanent deformation and flow of a-Al_2O_3 sample. Scale bar, 100 nm. F, force vector. **(right)** Average simulated and average experimental (electron beam off) shear compression stress as a function of strain, while the inset shows a deformed sample after the test (scale bar, 100 nm). Note that the experimental true stress is a compound of mixed shear and compression loading. The simulation error bars show the maximum variation (minimum to maximum) measured with different strain rates (37.5×10^6 to 6.0×10^8 s^{-1}), while the experimental error bars show the standard deviation between samples. Images reproduced from [1] with permission from The American Association for the Advancement of Science.

oxide materials.

Chapter 4

Methods

4.1 Molecular dynamics methods

4.1.1 Classical molecular dynamics

Molecular dynamics method is a computational technique extensively employed in the fields of materials science, chemistry, and biophysics [76–78], operating as a deterministic approach grounded in Newtonian mechanics. The interatomic potential (IAP) can be determined either from dynamic *ab initio* calculations or from a semiempirical function, results in *ab initio* molecular dynamics (AIMD) or classical molecular dynamics, respectively. This method solves Newton's equations of motion to determine the positions, velocities, and interaction forces of atoms within the system, ultimately forecasting the system's state through successive iterations. Specifically, when given an initial setup, an atom's total potential energy is calculated as the overlap of the potential energies with all other atoms within a defined cutoff distance if a pair potential is utilized. The force vector between the selected pair of atoms is derived from the gradient vector computed based on the potential energy, and the total force vector can then be aggregated. Subsequently, the change in velocity is obtained by integrating the force vector over a specified time interval. Furthermore, the atom's positional change is determined by integrating the velocity over the same time interval. Figure 4.1 illustrates a schematic flowchart of a typical molecular dynamics simulation.

Since simulations are conducted on discrete time series, variance is an inevitable occurrence. Various time integration methods have been developed to enhance accuracy while keeping computational costs manageable. These include the Verlet algorithm, Leap-Frog algorithm, velocity-Verlet algorithm, and Gear (Predictor-Corrector) algorithm [79]. For instance, in the Gear algorithm, predictions for $r(t+\Delta t)$, $v(t+\Delta t)$, $a(t+\Delta t)$, and additional terms are made at a specific time t

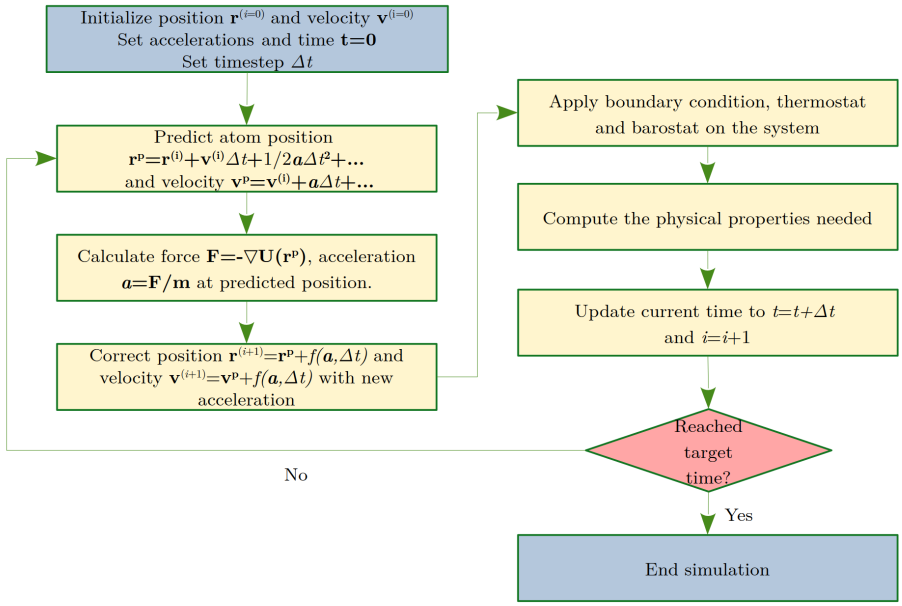


Figure 4.1: Flowchart of a typical Molecular dynamics simulation.

using Taylor's expansion. Corrections are then applied using the newly calculated $a^C(t+\Delta t)$ at the predicted $r(t+\Delta t)$.

In contrast, the velocity-Verlet algorithm represents an enhanced version of both the Verlet and Leap-Frog algorithms. While the velocity-Verlet algorithm may exhibit more noticeable local fluctuations in the energy profile, it generally maintains energy conservation more effectively than the Gear algorithm when utilizing the same time step Δt. Hence, the velocity-Verlet algorithm is often a preferred choice for time integration in various scenarios and is commonly utilized in molecular dynamics simulation software like LAMMPS [80]. Figure 4.2 illustrates a diagram of the iteration process of the Velocity-Verlet algorithm. Starting with time t and the atom's position $r(t)$, velocity $v(t)$, and acceleration $a(t)$, we first compute

$$r(t+\Delta t) = r(t) + \Delta t v(t) + \frac{1}{2}\Delta t^2 a(t), \tag{4.1}$$

$$v(t+\frac{1}{2}\Delta t) = v(t) + \frac{1}{2}\Delta t a(t), \tag{4.2}$$

based on the new $a(t+\Delta t)$ derived from $r(t+\Delta t)$, $v(t+\Delta t)$ can be calculated as

$$v(t+\Delta t) = v(t+\frac{1}{2}\Delta t) + \frac{1}{2}\Delta t a(t+\Delta t) \tag{4.3}$$

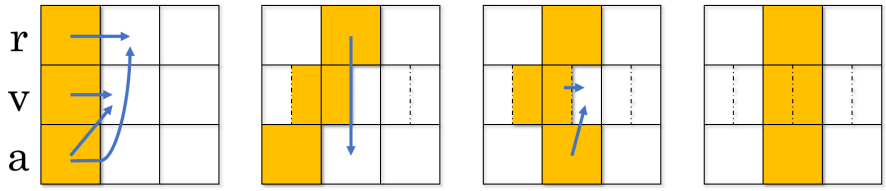


Figure 4.2: Schematic of velocity-Verlet time integration, columns indicate adjacent time points in the simulation. r, v and a mean position, velocity, and acceleration.

Temperature and pressure control

During MD simulations, it is essential to maintain the system under a specific ensemble to mimic experimental settings accurately. Examples of these ensembles include the microcanonical ensemble (NVE), canonical ensemble (NVT), and constant-temperature constant-pressure ensemble (NPT). The choice of ensemble determines whether the system is isolated or can exchange energy with the surroundings and if the system can alter its volume. These ensembles can replicate various real experimental conditions encountered in mechanical tests. For instance, simulating adiabatic conditions corresponds to the NVE ensemble, while simulating diabatic conditions aligns with the NVT or NPT ensembles. In terms of pressure, simulating confined deformation is akin to the NVE or NVT ensembles, whereas simulating unconfined deformation is akin to the NPT ensemble.

From a microscopic perspective, temperature is a statistical description of the energy of motion of atoms, described in the equipartition theorem as

$$< \frac{1}{2} m_i v_{i,\alpha}^2 >= \frac{1}{2} k_B T, \tag{4.4}$$

where k_B is the Boltzmann constant, $v_{i,\alpha}^2$ is the velocity of atom i in α degree of freedom. Therefore, control of the temperature can be achieved by controlling the velocities of the atoms, and multiple algorithms have been developed to achieve this goal. For example, the Berendsen thermostat controls temperature by building a weak coupling between atom velocities and temperature [81]. The temperature would slowly dampen to the desired temperatures. This method does not require the system to be very close to equilibrium, but does not sample the canonical ensemble. On the contrary, the Langevin thermostat is a stochastic method that controls the temperature by giving the atoms a random force at each time step to drive the atoms to the desired temperature [82]. By carefully choosing the random forces and friction terms, this algorithm could give the right fluctuations so that the thermostat will work as well at NVT. However, because of the introduction of a random force, properties such as diffusion coefficient will be incorrectly calculated. Another thermostat algorithm is the Nose-Hoover thermostat [83]. This creates an imaginary heat bath region and treats the combination of real and extended regions as a large NVE ensemble. Compared to the

weak coupling of the Berendsen algorithm, the Nose-Hoover thermostat is much softer and should only be applied if the system is close to equilibrium conditions.

Similarly to temperature, if we view the system from a microscopic perspective, pressure is the result of a tremendous amount of atomic collisions in a certain direction. Therefore, controlling the pressure can be achieved similarly to controlling the temperature. To drive the system toward the desired pressure, we need to modify either the temperature or volume, usually the latter. The Berendsen algorithm mentioned above and the Nose-Hoover algorithm can also be implemented here. Similarly, the Nose-Hoover barostat should be used under close-to-equilibrium conditions, while the Berendsen algorithm can be used under wider conditions.

Moreover, we should acknowledge that it is almost impossible to deform a sample at significantly high strain rates without causing an increase in the temperature. The effects of such a temperature rise caused by a high strain rate are called adiabatic heating and have been widely investigated experimentally [84–86]. However, the strain rates used in experiments are not even close to those strain rates used in simulations. Although we could set the simulation as realistic as possible by using the NVE ensemble during deformation, the immediate liquification that happens consequently will make the results meaningless. Therefore, it is worth noting that the simulation conditions are ideal for the heat to dissipate immediately.

4.1.2 Interatomic potentials

Different types of potentials

The interatomic potential, also known as the interatomic force field, is typically a semiempirical equation. Its application in simulations is theoretically supported by two primary assumptions: firstly, the system's total energy can be viewed as the sum of individual atomic energies, and secondly, there exists a finite interaction distance. The energy and forces acting on the atoms can be derived from the selected potential during molecular dynamics simulations. Numerous analytical models have been devised to characterize this potential. Among them, the pair potential stands out as one of the simplest types, depending solely on the distance between two particles as a variable. For instance, the Lennard-Jones potential, despite its simplicity, can effectively model noble gas systems. More intricate versions of pair potential models, such as the Buckingham form potential, can even be applied to charged systems. Nonetheless, there are scenarios where pair potentials fall short in accurately representing the system's energy. To address this, many-body potentials have been introduced. These models incorporate additional variables like bond angles, besides interatomic distances, to better capture the atomic configuration. The Embedded Atom Method (EAM) potential, a many-body potential, is particularly valuable for simulating metals. It comprises a two-body term and a many-body term known as the embedding

Table 4.1: Potential parameters of Coulomb-Buckingham potential for a-Al_2O_3 obtained using the parameter values and combination rules from Matsui [87].

	A (eV)	ρ (Å)	C (eV·Å^6)
Al-Al	31571310.74	0.068	14.05114560
Al-O	28477.25737	0.172	34.57833522
O-O	6462.75033	0.276	85.09350771

	Mass (u)	Charge (C)
Al	26.9815	1.4175
O	15.9994	-0.9450

term. In this context, the electronic density at a specific point is approximated as the linear overlap of all atoms within the system.

The choice of potential is also decisivively influential in the accuracy of the calculation. The interatomic potential can be created using mathematical expressions to fit a large number of DFT calculation data. The potential function of the Buckingham form used in this work has the following general form:

$$U_{ij}(r_{ij}) = \frac{Z_i Z_j}{4\pi\epsilon_0}\frac{1}{r_{ij}} + Ae^{-r_{ij}/\rho} - \frac{C}{r_{ij}^6}, \tag{4.5}$$

where U_{ij} represents the pair potential between atoms i and j, Z_i and Z_j denote the effective charges of the atoms, ϵ_0 stands for the vacuum permeability, r_{ij} indicates the distance separating atoms i and j, and A, ρ are repulsion potential parameters while C is the Van der Waals constant. The parameters utilized for the alumina and silica simulations by Matsui [87] and BKS [88] are presented in Tables 4.1 and 4.2, respectively. In the silica simulation, it was observed that the BKS potential function generates a potential well at a short distance. At elevated temperatures, atoms might surpass the barrier and descend into this potential well, leading to system instability. To prevent this, the original potential function can be truncated at close distances, and the repulsive force of proximity can be represented using a Ziegler-Biersack-Littmark (ZBL) potential [89], a harmonic function, or a polynomial function. In this study, a harmonic function is employed to adjust the Si-O component, and the specific approach is detailed in Ref. [33].

Table 4.2: Potential parameters of Coulomb-Buckingham potential for a-SiO_2 obtained using the parameter values and combination rules from van Beest *et al.* [88]

	A (eV)	ρ (Å)	C (eV·Å^6)
Si-O	18003.7572	0.2052	133.5381
O-O	1388.773	0.36232	175.0

	Mass (u)	Charge (C)
Si	28.0855	+2.4
O	15.9994	-1.2

Summation of the Coulombic part

In ionic systems, ions could have positive or negative charges, which leads to the Coulomb force between ions. Coulomb potential can be described as

$$U_{\text{Coul}} = \frac{e^2}{4\pi\varepsilon_0}\frac{Z_i Z_j}{r_{ij}}, \tag{4.6}$$

where Z_i and Z_j are the effective charges of the atoms, ε_0 is the vacuum permeability, and r_{ij} is the distance between the atoms i and j. Unlike short-range potentials that converge quickly with pair distance, we know that the Coulomb potential is not convergent since it scales as r^{-1}. This makes the summation of the electrostatic energy over periodic boundary conditions impossible. A widely used Ewald summation could effectively handle this divergent summation. The original Coulomb potential is now written as

$$U_{\text{Ewald}} = U^r + U^s + U^k, \tag{4.7}$$

where U^r is the electrostatic potential at real space, U^s is the self-interaction term and U^k is the reciprocal space term. The Ewald summation works as follows: for each point charge in the system, it is replaced by a Gaussian charge distribution centered at each ion and has the total charge opposite of the ion's charge. By performing the Fourier transformation, the potential energy and force of the Gaussian charge distributions can be calculated efficiently in reciprocal space.

The Particle-Particle Particle-Mesh (PPPM) method was developed from the Ewald summation. Instead of performing the calculation in reciprocal space directly, the Gaussian atom charge is mapped to a 3D grid. Fourier transform is performed on each grid to solve Poisson's equation and get the potential at the grid point. Then the potential is interpolated into the real space [90, 91]. For a N-atom system, the Ewald summation has a time complexity of $O(N^{\frac{3}{2}})$, while the PPPM method could achieve a time complexity of $O(NlogN)$. If the atom number is huge, the PPPM method could effectively reduce the time cost of simulation.

Kernel-based machine-learning potential

In recent times, the advancement of machine learning (ML) techniques has impacted the evolution of interatomic potentials [92]. The kernel-based machine learning approach or the deep learning method using neural networks can be employed for potential development, with only the former being utilized in this

study. The creation of a dependable kernel-based machine learning potential involves several crucial steps. Initially, it is imperative to provide ample training data encompassing a wide range of configurations. Typically, training and validation of a machine learning potential requires a vast quantity of data based on DFT calculation [93].

In this work, training data for variant Ga_2O_3 configurations is prepared, including dimers, trimers, various crystalline structures, and uncommon high-temperature liquid-phase clusters. The database can be adjusted or refined during training iterations until the potential meets the desired quality standards. Two forms of ML interatomic potentials are developed for a-Ga_2O_3, namely soapGAP and tabGAP [39], between which different descriptors are used. During training, descriptor plays a vital role as it determines how the training data is chracterized. Choosing of it is a trade-off between accuracy and efficiency. A simpler descriptor has fewer hyperparameters, it can yield a potential akin to existing many-body potentials, rendering the machine learning process akin to fine-tuning conventional potentials [94, 95]. Conversely, a more intricate descriptor results in a more complex potential, albeit at the expense of increased computational resources due to the higher number of hyperparameters involved in the training process [96, 97].

4.1.3 Modeling the quenching process and mechanical tests with molecular dynamics simulation

Classical molecular dynamics simulations in this work are performed using the LAMMPS code [80]. Computational simulation of the quenching process is performed to prepare the amorphous structure. The initial structure is heated and equilibrated at a high enough temperature to erase the crystalline structural memory. Then the structure, usually in the liquid phase, is cooled to room temperature at a constant cooling rates (q). Cooling rate has been reported being able to affect the formed amorphous structure [19, 28, 33, 98]. Therefore, it is used as a variable in this work to investigate the influence on the formed amorphous structure. The Nose-Hoover algorithm is used to control temperature and pressure. Periodic boundary conditions are applied during the quenching simulation, and amorphous structures prepared under such conditions can be regarded as bulk. Properties of the system such as potential energy, volume, and temperature are monitored for future estimation of glass transition temperature.

The mechanical tests, including compression and tension, are then performed. The strain is applied in one direction, and the NPT ensemble is applied in other directions to automatically adjust the total volume, using the Nose-Hoover algorithm. The deformation is achieved in such a way that the size of the simulation box is changed every certain number of timesteps. The discontinuity of the deformation will become more obvious with a time interval. Re-mapping of the atom coordinates and velocities in the system is usually performed to reduce the

effect of this discontinuity. However, instead of such a compromise, in this work, the smallest possible time interval (1 fs) is used and artificial remaps are turned off to make the results as realistic and accurate as possible. During mechanical test simulations, the properties of the system such as volume, potential energy, and stress are monitored. Per atom information is dumped for later structural analysis.

Simulation settings such as system size, cooling rate, and strain rate are carefully chosen to avoid causing any artefact [25, 98–100].

4.2 Structural analysis methods

To analyze the simulation results, we used atomic-level methods such as coordination analysis, radial distribution function (RDF) analysis, and bond angle distribution (BAD) analysis. We also used methods that can capture medium-range structural information, such as $D^2_{\min}$ analysis and polyhedral analysis. Coordination analysis, RDF and BAD analysis, and $D^2_{\min}$ analysis are all performed using Ovito software [101], polyhedral analysis is a coarse-grained analysis method which is originally proposed in this work.

Radial distribution function

The radial distribution function $g(r)$ is the average distribution of atoms around a center reference atom. It is defined as:

$$g(r) = \frac{\rho(r)}{\rho}, \tag{4.8}$$

where $\rho(r)$ is the local atomic density at distance r, ρ is the atomic density of the spherical region within the analyzing cutoff distance. When implementing the equation, $g(r)$ is the ratio between the number of atoms in the shell at distance r and the number of atoms calculated from the global atomic density. For a binary system with atom types X and O, the radial distribution function can be calculated from the partial RDFs as

$$g(r) = c_{\mathrm{X}}^2 g_{\mathrm{XX}}(r) + 2c_{\mathrm{X}}c_{\mathrm{O}}g_{\mathrm{XO}}(r) + c_{\mathrm{O}}^2 g_{\mathrm{OO}}(r), \tag{4.9}$$

where c_{X} means the concentration of atom type X, and $g_{\mathrm{XO}}(r)$ is the partial RDF between atom type X and O. Factor 2 here is because $g_{\mathrm{XO}}(r) = g_{\mathrm{OX}}(r)$.

Coordination analysis

For each atom, the coordination number is the number of atoms within a certain cutoff distance. When choosing the cutoff distance, a general rule is to pick from the radial distribution function and use the first minimum of the RDF.

Bond angle distribution

The bond angle is formed by two bonds and one center atom, that is, three atoms, to obtain a bond angle. Bonds are calculated as in the case of coordination analysis.

Non-affine displacement

D^2_{min} is the minimum value of the square of the local atomic displacement (D^2) and describes the local deviation from affine deformation compared to a reference configuration, as introduced by Falk and Langer [102]. It is a descriptor of local plastic deformation and is used to capture plastic deformation during tensile tests. D^2 is the sum of squares of residuals when fitting a data set according to the least squares principle, and the expression of D is

$$D = |\mathbf{R} - J\mathbf{R_0}|, \tag{4.10}$$

where $\mathbf{R}$ are the displacement vectors from the center atom to the atom within the cutoff distance at the current configuration and $\mathbf{R_0}$ are the displacement vectors at the reference configuration. J is the deformation gradient tensor that links the current and reference configurations. Calculating the J that minimizes D^2 involves calculating the derivative of the matrix. We have

$$J = (\mathbf{R_0}^{\mathrm{T}}\mathbf{R_0})^{-1}\mathbf{R_0}^{\mathrm{T}}\mathbf{R}, \tag{4.11}$$

so that we have

$$D^2_{min} = |\mathbf{R} - J\mathbf{R_0}|^2, \tag{4.12}$$

where J is known.

The cutoff distance (r_{cut}) should be set first when computing D^2_{min}. It defines the distance within which the displacement vector will be constructed. A larger r_{cut} can include more atoms in the calculation so that D^2_{min} can be a medium-range indicator of localized strain. But a large r_{cut} may also reduce the resolution of this characterizing method because the results would be smoothed over space. A too small r_{cut} should also be avoided because it leads to large variances between atoms and produces extra noise to the characterizing results. Therefore, we chose twice the bond length as the cutoff value when analyzing the results, which balances the resolution and the noise, as

$$r_{cut} = 2l, \tag{4.13}$$

where r_{cut} is the cutoff distance for D^2_{min} calculation and l is the bond length. The bond length is chosen as the first minimum on the RDF in our simulations. Depending on whether the reference configuration is a fixed frame of the initial structure or a moving frame with a fixed interval before the given configuration, we have cumulative D^2_{min} and momentary D^2_{min}, respectively.

Localized plastic strain event

To distinguish the atoms in a viscous flow, they should first have a momentary D^2_{min} large enough. A threshold value is needed and should be dynamic because the D^2_{min} results are constantly changing. After trying different values, we choose twice the average momentary D^2_{min} as the threshold value. Since the positions of atoms are dumped with a certain interval during simulations, the threshold value would also change accordingly.

$$d = 2\overline{D^2_{min}}, \tag{4.14}$$

Based on this value a close enough matching is reached between the selected atoms and the high momentary D^2_{min} atoms in the visualizations. From the visualization we can see that viscous flow regions can have several nanometers in one dimension and can have hundreds of atoms. As a result, we set the lower limit of the cluster at 200 atoms when performing the cluster analysis on the high momentary D^2_{min} atoms. The definition of viscous flow is artificial in this study, but since here we care more about how the results would react to the change in strain rate, the definition of viscous flow will not be discussed further.

Polyhedral analysis

Structural analysis methods include polyhedral analysis and ring statistics analysis. Both methods require frequent construction of neighbor lists, and the complexity of construction analysis is $O(N^2)$, where N is the total number of atoms in the system. When the structure to be analyzed is relatively large, the resources consumed quickly become unbearable. The cell index method is a widely used algorithm in MD codes to solve this problem, which has been implemented in the analysis tools as well. First, the simulation box is divided into cells with each dimension not smaller than the set cutoff value. Then each atom is sorted into corresponding cell by its coordinate. Consequently, we can look for neighbors of an atom in the cell it is in and the neighboring cells. In this way, the complexity of the calculation process is reduced to approximately $O(N)$. A Fortran code was developed to achieve efficient analysis of the simulation results [103].

The polyhedral analysis we performed in this work is a coarse-grained analysis of the system. By polyhedra, we refer to the basic structure with a cation as its center and oxygen atoms bonded to the system as the corners. By linking the corner oxygen atoms, we can get a polyhedron structure. The polyhedral analysis is about the second nearest atoms and contains more information than the coordination analysis. Unlike atomic bonds, neighboring polyhedra can be further classified according to how they connect to each other. In practice, two polyhedra are neighbors if they have shared oxygen atoms in their neighbor list. The number of shared oxygen atoms determines whether they are connected by sharing a corner (one shared oxygen atom), an edge (two shared oxygen atoms) or a face (three shared oxygen atoms). As illustrated in Figure 4.3, on the basis

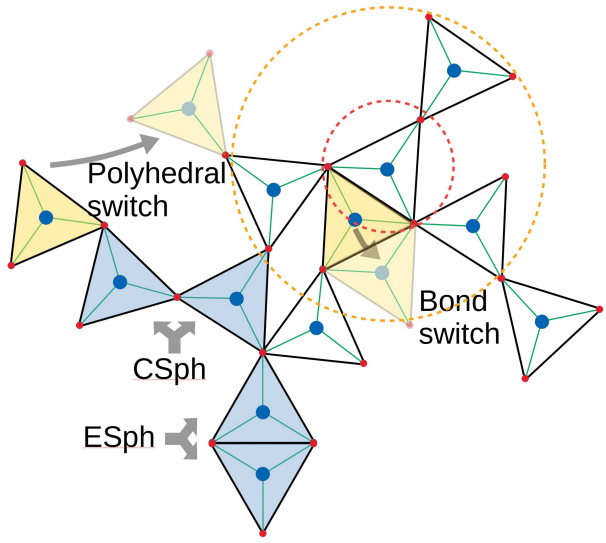


Figure 4.3: 2-D schematic of oxide glass polyhedra with different topological status. Cation atoms are colored blue, oxygen atoms are colored red, cation–oxygen bonds are shown as blue lines, and black lines are the edges of fictive polyhedra. Edge-sharing polyhedra and corner-sharing polyhedra are distinguishable in this figure. Polyhedral neighbor change and bond change are illustrated with arrows. The red dashed-line circle indicates the scale of information conveyed by bond switching analysis, i.e. the scale of individual atom bonds (short-range order), and the yellow dashed-line circle indicates information that coarse-grained analysis could disclose, i.e., the scale of neighboring polyhedra. From Publication III, images reprinted according to the creative commons license CC BY 4.0.

of the maximum number of shared oxygen atoms with their neighbors, polyhedra are termed corner-sharing polyhedra (CSph), edge-sharing polyhedra (ESph), and face-sharing polyhedra (FSph), respectively. Because FSph is rarely observed in our simulation results, it is neglected in our analysis.

A polyhedral neighbor change event(PNCE) is the neighbor change between two adjacent polyhedra and two continuous frames, that is, the exclusive disjunction of the polyhedral neighbor list between reference and current configuration. According to the type of polyhedron before and after the PNCE, it can be classified into four possible types. To obtain a time-independent result, PNCE is normalized by the strain interval between two frames, and we have

$$P_{CSph} = \frac{PNCE_{ESph}^{CSph} + PNCE_{CSph}^{ESph} + PNCE_{CSph}^{CSph}}{N_{CSph}\Delta\varepsilon} \tag{4.15}$$

$$P_{ESph} = \frac{PNCE_{CSph}^{ESph} + PNCE_{ESph}^{CSph} + PNCE_{ESph}^{ESph}}{N_{ESph}\Delta\varepsilon}, \tag{4.16}$$

where P is the normalized number of events per $\Delta\varepsilon$ strain change, PNCE^{CSph} means it is a CSph before the event, PNCE_{ESph} means it is an ESph after the

event, $\Delta\varepsilon$ is the strain increment between two adjacent configurations, and N_{CSph} means the total number of polyhedra type CSph after the increment.

Ring statistics

Ring statistics analysis is performed with the algorithm developed by Yuan and Cormack [104], which gives the statistics of the primitive rings. The statistics are calculated from an Al atom, and hops are counted from an Al to an Al atom via a bonded oxygen atom. For a certain atom in the system, the breadth-first algorithm is used to obtain the local ring structures. The cutoff radius is determined from the first minimum on the RDF.

Chapter 5

Atomistic simulation of room temperature plasticity of oxide glass materials

5.1 Dependence of glass transition temperature on cooling rate

Alumina has a long history of application as a ceramic. However, its amorphous state is still poorly studied. In Publication I, we first confirmed the glass transition process of Al_2O_3 and estimated the glass transition temperature (T_g) with molecular dynamics simulations. Then we investigated the influence of the cooling rate (q) on the resulting amorphous structure. We found in our simulations that at $q = 1 \times 10^{10}$ Ks^{-1}, crystallization of alumina occurs instead of amorphization, indicating that a higher q must be used to computationally prepare a-Al_2O_3. This cooling rate is much higher than that of ordinary glass formers, confirming the harsh conditions needed to prepare this amorphous material.

We prepared nine amorphous Al_2O_3 structures with q varying from $1{\times}10^{11}$ to $5{\times}10^{13}$ Ks^{-1}. In addition, a special structure is prepared in such a way that energy minimization is performed on the 4000 K melt directly using the conjugate gradient algorithm. The obtained structure is regarded as quenched with a cooling rate approaching infinity in later analysis. T_g is not estimated from this simulation but the obtained structure is used in later tensile tests. The results of the quenching simulation verified that Al_2O_3 can be prepared amorphous through melt-quench, indicates that it is a glass. For glass, T_g is an important property that can be determined in multiple ways. Here, we determined the T_g of a-Al_2O_3 from the potential energy (E_p) change during quenching, as the intersection point of the linear fittings of the E_p - T curve's high- and low-temperature

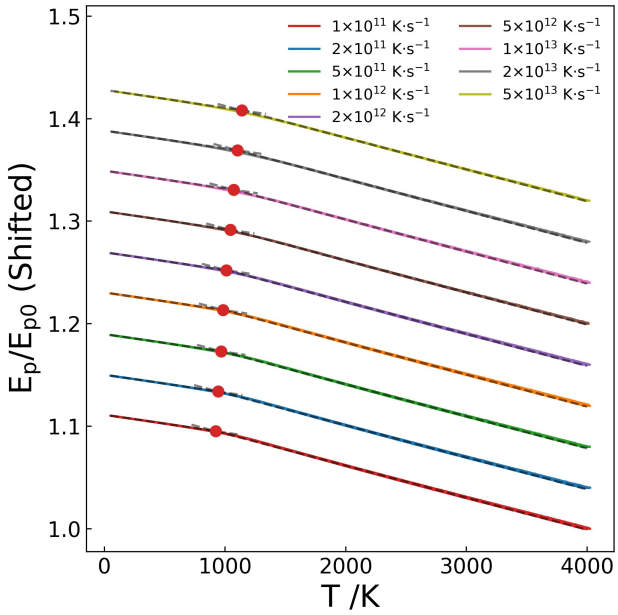


Figure 5.1: The potential energy of Al_2O_3 as a function of temperature. Energy is scaled by the potential energy of the 4000 K liquid (E_{p0}). Curves with different cooling rates are shifted for clarification. The glass transition temperatures T_g are calculated as the intersections of the separate linear fits of the potential energy curves (gray dashed lines) and are marked with red circles. From Publication I, images reprinted according to the creative commons license CC BY 4.0.

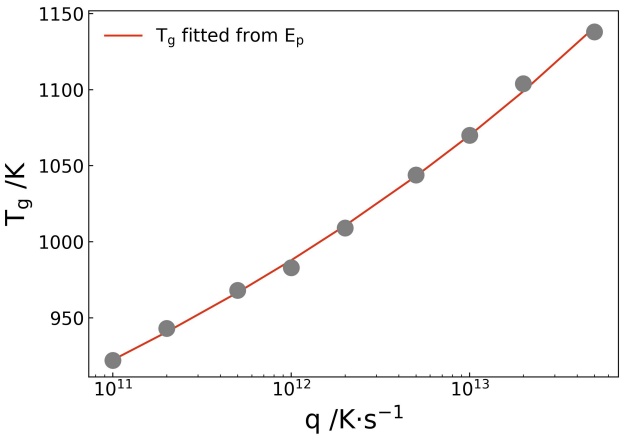


Figure 5.2: Glass transition temperature determined from the potential energy as a function of cooling rates (markers) and fit of the data to Eq. 5.4 (line). From Publication I, images reprinted according to the creative commons license CC BY 4.0.

part, as shown in Figure 5.1. We see that from the slowest to the fastest q, the obtained T_g increases from 930 to 1180 K. The correlation between the (q) of the glass material and the glass transition temperature (T_g) has been modeled in multiple forms [55]. The Vogel-Fulcher-Tammann equation (VFT) [105–107] is used in this work to construct a practical model that can be used to describe the q - T_g correlation of a-Al_2O_3, similar to the work done for a-SiO_2 [33]. It is a semiempirical equation derived from the Arrhenius law of the relaxation time of atoms in a viscous liquid. Derivation of the q - T_g form of the model (Eqs. 5.1) is based on the Maxwell's expression for relaxation time (Eqs. 5.2), and the inverse correlation between relaxation time (τ) and q (Eqs. 5.3):

$$\eta = A \exp \frac{B}{T - T_0}, \tag{5.1}$$

where η is viscosity, T is temperature A, B and T_0 are fitting parameters.

$$\tau = \frac{\eta}{G_\infty}, \tag{5.2}$$

where G_∞ is the instantaneous shear modulus.

$$\tau = \frac{T_1}{q}\bigg|_{T=T_g}, \tag{5.3}$$

where T_1 is a constant. The fitting function for the VFT model is

$$T_g = T_0 - \frac{A}{\exp(Bq)}, \tag{5.4}$$

where A and B are constants, and T_0 is the limiting value of T_g in the infinitesimal cooling and heating rates. Fitting results are shown in Figure 5.2. Although the findings suggest that the VFT equation might be suitable for describing the connection between T_g and q of alumina, there are still notable concerns. Firstly, Angell *et al.* [55] suggested that q should span up to ten orders of magnitude to thoroughly validate the behavior of the VFT equation, a range much wider than the two and a half orders of magnitude we have. Secondly, the VFT equation is typically effective for "strong" glass formers, whereas alumina is likely a "fragile" glass former [108]. In conclusion, characterizing the q - T_g relationship of a-Al_2O_3 is complex due to the challenge of obtaining extensive T_g data across a broader range of q. At relatively low cooling rates ($< 10^{10}$ Ks^{-1}), material crystallization occurs, while at high cooling rates ($> 10^{13}$ Ks^{-1}), the material's behavior may deviate from reality.

We then perform tensile simulations on the samples quenched at different q with a constant strain rate of 1×10^9 s^{-1}. In Figure 5.3 we show that at all cooling rates, the obtained structures exhibit plastic deforming ability and can withstand 50% engineering strain without fracture. This agrees with the previous experimental observation [1]. With the increase of q, the height of the hump (σ_{max}-σ_{flow}) on the stress-strain curve decreases from 3.5 GPa at the slowest q to 0 at the infinite cooling rate. When the structure is quenched at a lower cooling rate, atoms

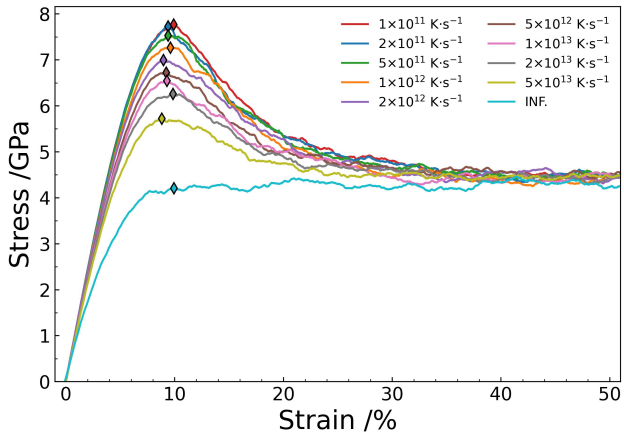


Figure 5.3: Stress-strain plot of systems quenched with q ranges from 1×10^{11} Ks^{-1} to 5×10^{13} K/s stretched in 300K. The maximum stresses and strains ($\sigma_{\max}$, $\varepsilon_{\max}$) are marked with diamond markers. From Publication I, images reprinted according to the creative commons license CC BY 4.0.

are given more time to probe low energy points. Consequently, the stretching process requires more mechanical energy input to force the atom to leave its original position. As the tensile deformation continues, the system reaches a new equilibrium and finally reaches flow stress. These results show that varying cooling rates would lead to different structures at the end of quenching process, and the structural differences consequently result in different mechanical properties. Characterization of the structures is needed to have a deeper understanding of the structural differences formed during the glass transition.

When estimating the glass transition temperature, we already noticed that the cooling rate can affect the density of the sample. To begin with, we have the results of the radial distribution function (RDF) and the bond angle distribution (BAD) (Figure 5.4). RDF results converge to $g(r) = 1$ at long distances, and the bond angle distributions do not show sharp peaks, indicating that the structures obtained are in an amorphous state that exhibits no long-range ordering. However, these two methods show almost negligible differences for different cooling rates, which means that they do not distinguish subtle structural differences.

Further characterization methods include coordination analysis, polyhedral analysis, and ring statistics analysis. These methods produce quantitative differences because they focus on different length scales when applied in the analysis. Figure 5.5 presents the results of these analyses. Coordination analysis first shows short-range structural differences between quenched structures. When q changes from 1×10^{11} Ks^{-1} to infinite, the maximum difference of oxygen fraction is 5.87% for 2-fold coordinated, and that of aluminum is 6.80% for 4-fold coordinated. The trend is that when q increases, atoms become more closely packed, and as the structures are elongated, the coordination decreases in all structures.

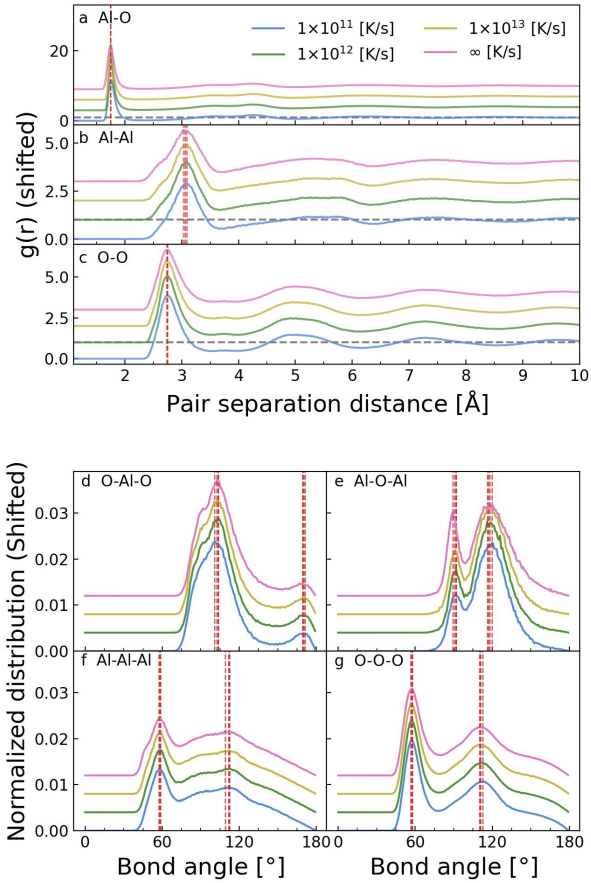


Figure 5.4: (a-c) Partial radial distribution functions of (a) Al-O pairs, (b) Al-Al pairs, and (c) O-O pairs for structures quenched with different cooling rates. Gray horizontal dashed lines represent $g(r) = 1$ which describes the absence of long-range order. Curves are labeled by their cooling rates and '∞' denotes the infinitely fast cooling. (d-g) Normalized bond angle distribution of (d) O-Al-O angles (e) Al-O-Al angles (f) Al-Al-Al angles (g) O-O-O angles. The cutoff distances for Al-Al, Al-O and O-O of 3.8, 2.3 and 3.4 Å, respectively, are used. From Publication I, images reprinted according to the creative commons license CC BY 4.0.

Compared to coordination analysis, polyhedral analysis includes the information of the second nearest neighbors and thus can reveal more information about the medium-range structure. The results show more significant differences when investigating the effect of the cooling rate on the structures. The maximum difference in the edge-sharing polyhedron (ESph) fraction is 7.61%, which is larger than the maximum difference between the results of the coordination analysis. Furthermore, the results of the polyhedral analysis capture a stress crossover during the tensile tests, indicating a possible transition state of the structure during the plastic deformation. The edge-sharing polyhedron fraction is the lowest at maximum stress, matching the stress-strain curves exhibiting a maximum at the

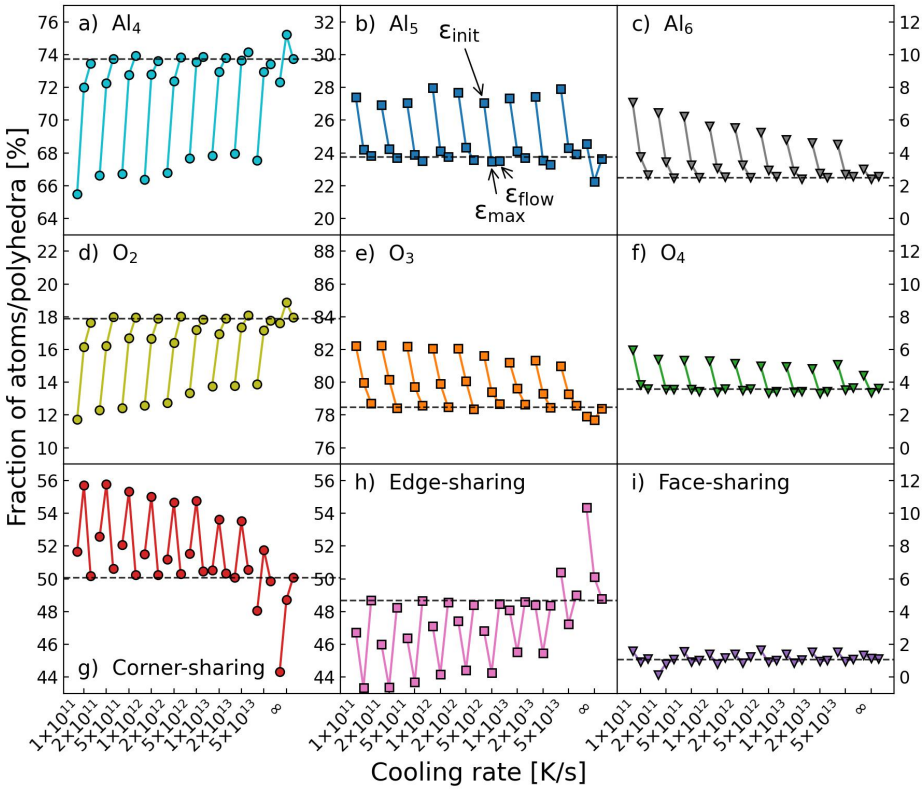


Figure 5.5: Coordination of (a-c) Al (d-f) O atoms and (g-i) polyhedron type computed for all systems at their initial, maximum stress, and flow stress (at 50% strain). The three connected markers from left to right denote the initial, maximum and flow stress for each atom or polyhedron type. The x-axis is the cooling rate used in creating the structure, the unit is Ks^{-1}, and the y-axis is the fraction of the total number of atoms or polyhedra equal to the number of Al atoms. For each data set, the dashed line shows the convergence of the results at flow stress. From Publication I, images reprinted according to the creative commons license CC BY 4.0.

same point. In explanation, at maximum stress the system resists plastic deformation to the highest point, and the fraction of the basic structures that can not easily deform is at the highest point.

As a topological characterization method, the results of ring statistics can also reveal the MRO of the structure, although the information provided by this analysis is not fully clear. As presented in Figure 5.6, the average ring size changes by 5.5% from the slowest to the fastest cooling rate. Moreover, it confirms the results of the polyhedral and coordination analysis that the structures converge to an identical structure at flow stress. Together with polyhedral analysis results, they show that characterizing methods focusing more on the medium-range structure are more likely to disclose the subtle differences between structures.

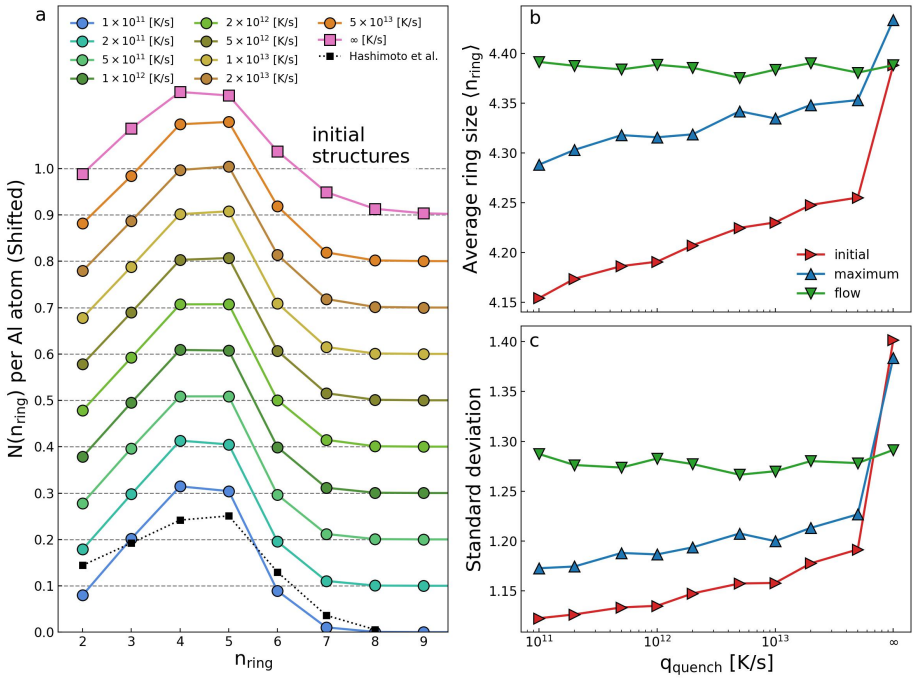


Figure 5.6: Ring statistics of a-Al_2O_3 structures quenched at different q. (a) Ring size distributions for different cooling rates. The solid black line results from Hashimoto *et al.* [109]. Results are shifted for clarity, and the horizontal dashed gray line is the baseline for each data set. (b) The average ring size for different cooling rates. Curves labeled 'initial', 'maximum' and 'flow' denote the data at $\varepsilon_{\text{init}}$, ε_{max} and $\varepsilon_{\text{flow}}$, respectively. (See Figure 5.3) (c) Standard deviation of the ring size distributions for different cooling rates. From Publication I, images reprinted according to the creative commons license CC BY 4.0.

5.2 Plastic deforming mechanism in amorphous alumina

After investigating the glass transition of alumina in Publication I, we are even more interested in its plastic deformation mechanism. To support the experimental study, atomistic simulations are performed to investigate the room temperature plastic deformation mechanism of amorphous alunima, presented in Publication II. The data obtained are characterized and analyzed in multiple ways.

On the experimental side, micropillar compression experiments are conducted first to investigate the mechanical behavior of amorphous alumina. We found that at room temperature the 2 μm-diameter micro-pillar samples could withstand up to 50% engineering strain without fracture when the experimental strain rate varies from 1×10^{-3} to 1×10^{3} s^{-1}. From the shape of the samples after the mechanical test, possibly different deformation mechanisms are hinted. In Figure 5.7 we clearly see that at relatively high strain rates, slip-like shear band

propagation occurred in the structures. At lower strain rates, more homogeneous plastic deformation can be observed and no shear band is observed.

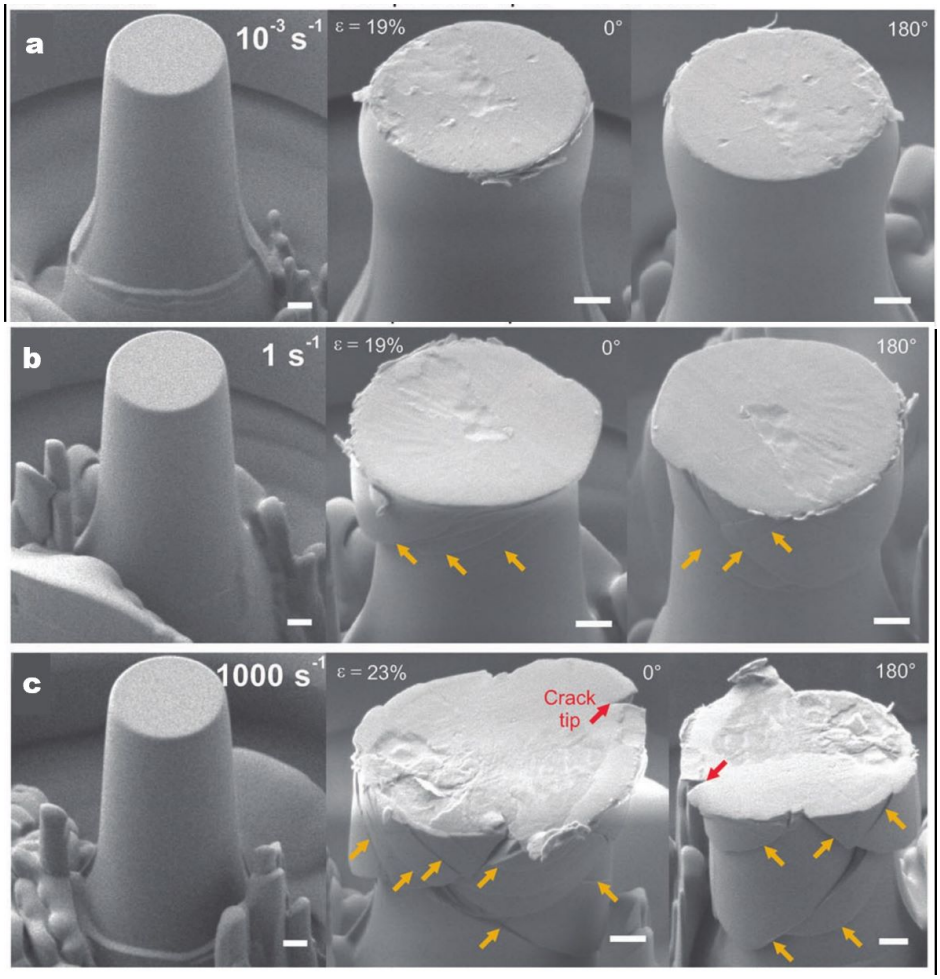


Figure 5.7: Micro-mechanical response of a-Al_2O_3 at room temperature. a) Strained by 19% at 10^{-3} s^{-1} strain rate, b) Strained by 19% at 1 s^{-1}, c) Strained by 23% at 1000 s^{-1}. The first sub-image shows the as-prepared micro-pillar, the second sub-image shows the deformed pillar, and the third sub-image shows the deformed pillar rotated 180°. The orange and red arrows show the locations of shear bands and crack tips, respectively. The scale bar is 400 nm. From Publication II, images reprinted according to the creative commons license CC BY 4.0.

To provide more information from a microscopic perspective, we investigated the compressive deformation of amorphous alumina with atomistic simulations. Bulk samples with approximately one million atoms and nanowire samples with approximately four million atoms are used in compressive test simulations, as schematically illustrated from Figure 5.8 to Figure 5.10. Bulk sample simulations

at different strain rates confirm that higher strain rates result in higher maximum stress and flow stress. These results align with the experimental results despite a huge gap in the magnitude of the strain rate.

From Figure 5.8 to Figure 5.10 we present the visualization results of the D^2_{min} analysis. We perform D^2_{min} analysis during compressive deformations to show the relative movement between atoms and the localized plastic strain. Cumulative and momentary D^2_{min} results for the nanowire sample, and momentary D^2_{min} results for the bulk sample are calculated.

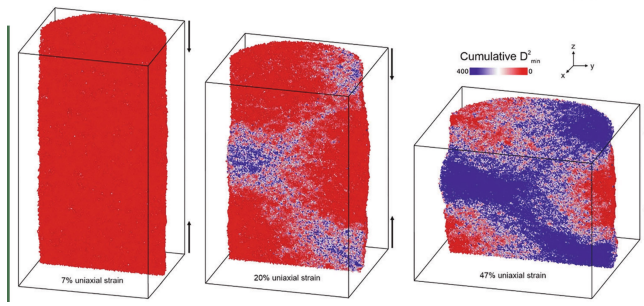


Figure 5.8: Vertical cross-sections of laterally unconfined PBC wire simulations under uniaxial compression measured at $\epsilon = 0.07$, 0.20, and 0.47. Atoms are colored by their cumulative D^2_{min} values from low(red) to high(blue). From Publication II, images reprinted according to the creative commons license CC BY 4.0.

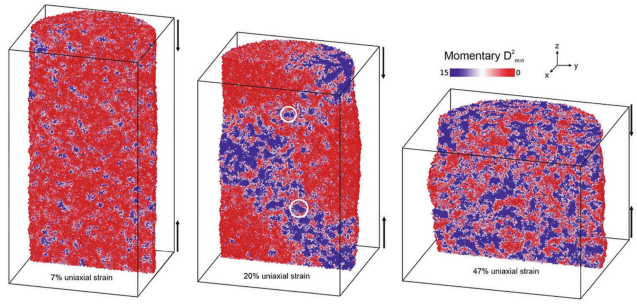


Figure 5.9: Vertical cross-sections of laterally unconfined PBC wire simulations under uniaxial compression measured at $\epsilon = 0.07$, 0.20, and 0.47. Atoms are colored by their momentary D^2_{min} values from low(red) to high(blue). From Publication II, images reprinted according to the creative commons license CC BY 4.0.

Cumulative D^2_{min} results in Figure 5.8 show clearly that there is shear banding in the strained nanowire structure. This 45-degree shear band is different from the dislocation 'slip' band that can be seen in crystals and is similar to the same concept that can be seen in metallic glass materials [67, 68]. Cumulative

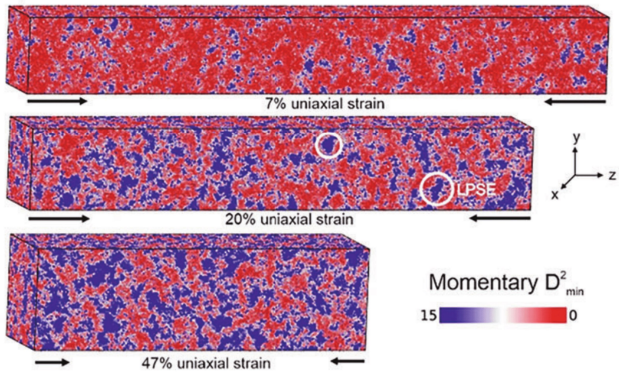


Figure 5.10: Confined bulk PBC simulations under uniaxial compression measured at $\epsilon = 0.07$, 0.20, and 0.47. Atoms are colored by their momentary D^2_{min} values from low(red) to high(blue). From Publication II, images reprinted according to the creative commons license CC BY 4.0.

D^2_{min} results show shear banding in every simulated structure. In comparison, momentary D^2_{min} can better reveal the dynamical viscous flow activity because it captures the localized plastic strain by comparing structures that have a constant time interval between them. Through visualizations of the tensile test results in Figure 5.9 and Figure 5.10, we see the appearance and disappearance of the high momentary D^2_{min} regions. Quantitative analysis of the systems shows that, despite different strain rates, the average momentary D^2_{min} values are close in the systems. The fraction of the high D^2_{min} atoms, *i.e.*, atoms that have D^2_{min} larger than twice the average D^2_{min}, is also very similar. This indicates that the total amounts of high D^2_{min} atoms do not depend on the strain rates thus their spatial distribution is the key factor. To further study the time dependence in the plastic deformation mechanism of amorphous alumina, the spatial distribution of the high D^2_{min} atoms must be analyzed deeply. We then tried to see the difference in the localized plastic strain event (LPSE) in the systems. It has been introduced earlier and is believed to play an important role during plastic deformation of a-Al_2O_3 [1]. Here, an LPSE is specifically defined as an atom cluster that has more than 200 high D^2_{min} atoms.

In contrast to the average momentary D^2_{min} results, a noticeable difference in the quantity of atoms in the LPSEs is observed at different strain rates, as depicted in Figure 5.11. The findings reveal a clear connection between stress and atom number in LPSEs. The number of atoms within LPSEs is greater at lower strain rates, suggesting the potential presence of larger and more numerous LPSEs at these strain rates. The increased atom count in LPSEs at lower strain rates leads to decreased stress, indicating that the formation of larger and more numerous LPSEs is an effective way of reducing stress during deformation. Furthermore, the results suggest that lower strain rates allow for more time for LPSE nucleation and growth. On the contrary, at higher strain rates, even though the overall quantity

of high D^2_{min} atoms is comparable, they do not have sufficient time to develop into large LPSEs. Hence, we posit that the time-limited LPSEs nucleation rate and their distribution during tensile deformation are two critical factors influencing plastic deformation ability.

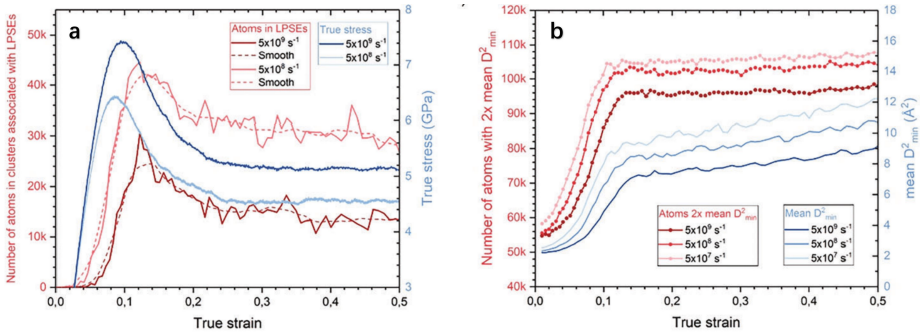


Figure 5.11: (a) Nucleation rate of LPSEs (left y-axis) and true stress (right y-axis) as a function of true strain in confined bulk PBC simulations. (b) Total amount of atoms in the confined bulk PBC simulations exhibiting a degree of local plasticity two times the mean D^2_{min} (left y-axis) and the mean D^2_{min}(right y-axis) as a function of strain at varying strain rates. From Publication II, images reprinted according to the creative commons license CC BY 4.0.

The results of this part verify the existence of room temperature plasticity in a-Al_2O_3 at micro-scale. The nucleation of LPSEs successfully mediates the plastic strain at the investigated strain rates. At higher strain rates, LPSEs tend to nucleate around the shear bands, leading to slip-like shear band propagation. While at lower strain rates, a more even distribution of the LPSEs can be observed, leading to more homogeneous plastic deformation. The nucleation rate of LPSEs was found to remain relatively constant at a constant temperature, which may explain the switch of the predominant mechanism at different strain rates, and ultimately mediated by the LPSE nucleation.

5.3 Understanding the plastic deformation mechanism from a coarse-grained level

Despite the ability to quantitatively investigate local atomic deformation, D^2_{min} analysis still has its shortcomings, it is sensitive to the cut-off value, and it is proportional to the total number of atoms within the cut-off distance. These factors make comparing different materials difficult. In this case, an original coarse-grained analysis is proposed to provide comparable results between different amorphous materials. This analysis method can bring about the following benefits. First, when focusing on the general connection mode, it can no longer be affected by the cutoff point and atomic coordination number. Second, more

information about MRO can be reflected in the analysis, which is essential for investigating the plastic deformation ability as we did in Publication I. In Publication III, we studied the brittle-to-ductile transition in normal and densified amorphous silica and analyzed the results with both D^2_{min} and coarse-grained analysis methods. Comparison of the results between amorphous alumina and amorphous silica deepens the understanding of the plastic deformation mechanism in oxide glass materials.

The brittle-to-ductile transition has been observed in amorphous silica before, and can be induced through various methods, such as densifying it by applying hydrostatic pressure during rapid cooling from a molten state. This characteristic of amorphous silica offers an opportunity to explore the crucial factor influencing its ability to deform plastically. Coordination analysis indicates that the distribution of coordination in amorphous silica is similar to that of alumina. By studying the transition from brittleness to ductility in amorphous silica, we may gain insights into the exceptional plastic deformation ability of amorphous alumina. Therefore, following a comprehensive examination of the plasticity of amorphous alumina at room temperature in previous studies, we aim to apply the same characterization techniques and theoretical framework to investigate amorphous silica.

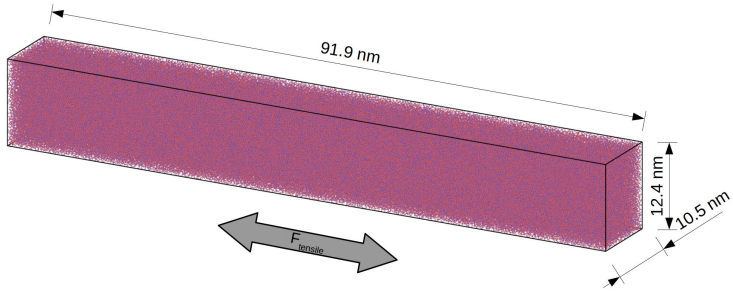


Figure 5.12: Schematic of the simulation box of a-SiO_2. Si and O atoms are colored blue and red respectively. From Publication III, images reprinted according to the creative commons license CC BY 4.0.

Amorphous SiO_2 structure is prepared in a melt-quench manner. It is cooled from 3000K to 300K at a constant cooling rate of 1 K/ps. The density of the structure is controlled by changing the hydrostatic pressure from 0 to 8 GPa. In Figure 5.12 we show a schematic of the prepared amorphous structure. The results show that when the quenching pressure increases from 0 to 8 GPa, the density of the amorphous silica sample increases by 35%. Figure 5.13 shows the schematic of amorphous Al_2O_3, which is also prepared in a melt-quench manner using the method described in detail in [110].

We first investigate the brittle-to-ductile transition with the structure. In simulations of tensile tests with a strain rate of 5×10^8 s^{-1}, the maximum stress value decreases as the quenching pressure increases for the densified samples, as presented in Figure 5.14. The normal a-silica sample breaks at approximately 17% strain. Fracture strain of amorphous silica samples delays with quenching pressure before 7 GPa. After 7 GPa, the sample can endure 50% strain without fracture, the same as the a-Al_2O_3 sample. We perform offloading simulations to verify that the presented yield is plastic rather than nonlinear elasticity. The results of the tensile test are characterized in multiple ways, static structural analysis means the characterization of the initial structures and dynamic analysis indicates the characterization of the structures during the tensile test.

In the static structural analysis part, the results of the polyhedral analysis show that the fraction of edge-sharing polyhedra (ESph) changes significantly as the quenching pressure increases, as shown in Figure 5.15. At 0 GPa, the sample is a random network of only tetrahedra connected by corner. However, in 8 GPa a-SiO_2, 7% of the polyhedra in the system are ESph. Additionally, we can regard a-Al_2O_3 locating on the extrapolation of this trend because it has over 50% edge-sharing polyhedra. As we have already investigated, amorphous alumina showed extraordinary room-temperature plastic deformation ability. We raise the question of whether plasticity in amorphous alumina is related to its high fraction of edge-sharing polyhedron and whether the brittle-to-ductile transition in amorphous silica is due to the increase of the edge-sharing polyhedra fraction. Answering this question can help us build up a universal understanding of the plastic deforming ability in oxide glass materials.

In this case, the coarse-grained analysis is proposed, and we used this tool to disclose details of the polyhedral level neighbor change during the tensile test. The results show that a structure that shows more plasticity, that is, has a larger fracture strain, the polyhedra in its system change their neighbors more frequently during the tensile test, as presented in Figure 5.16. We see that when the ESph fraction increases in amorphous silica, the number of polyhedral neighbor change

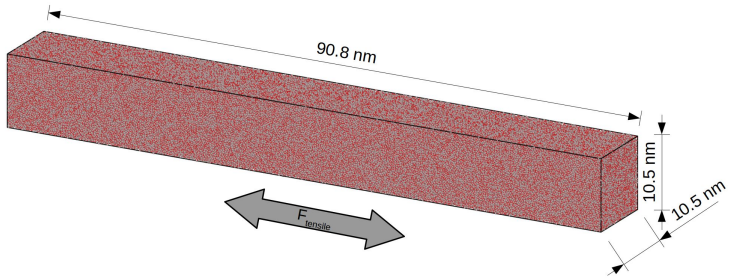


Figure 5.13: Schematic of the simulation box of a-Al_2O_3. O atoms are colored red. From Publication III, images reprinted according to the creative commons license CC BY 4.0.

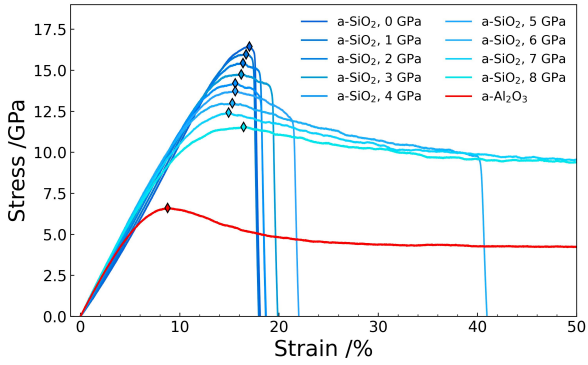


Figure 5.14: Stress as a function of strain for a-Al_2O_3 and for a-SiO_2 structures quenched at different pressures as obtained from 0 - 50% strain tensile test simulations. The maximum stress points of structures are marked with diamond markers. From Publication III, images reprinted according to the creative commons license CC BY 4.0.

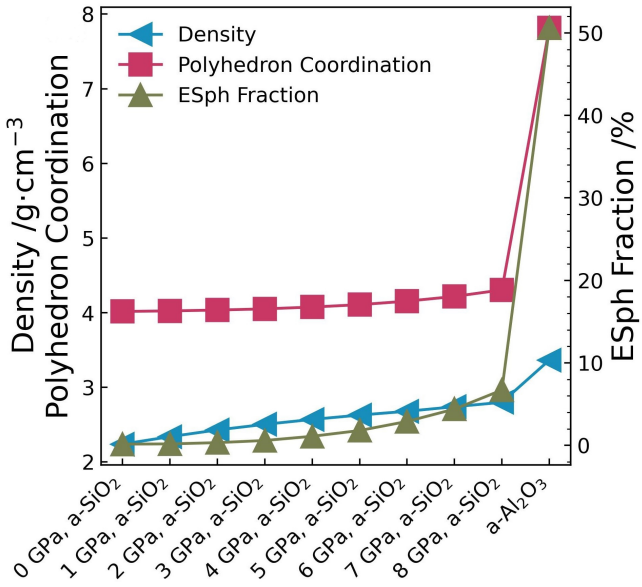


Figure 5.15: Density, polyhedron coordination, and ESph fraction of a-SiO_2 that quenched at different pressures and a-Al_2O_3. From Publication III, images reprinted according to the creative commons license CC BY 4.0.

events (PNCEs) also increases, and stronger plastic deformation ability is observed during deformation.

The importance of ESph during the tensile test can be better seen if we classify the neighbor change events more carefully according to the polyhedron type one event involved. We can see that edge-sharing polyhedra contribute more to

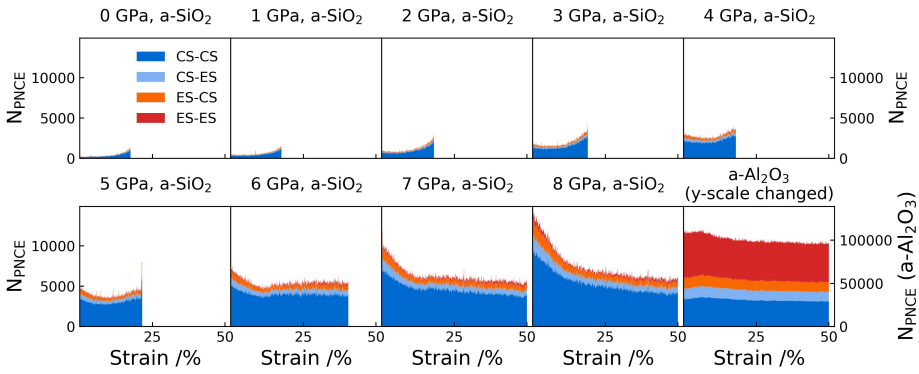


Figure 5.16: Types of polyhedral neighbor change events (PNCE) in all structures during the tensile test, where the x-axis is the engineering strain in percentage, the y-axis indicates the PNCE number. Four different types of PNCE are shown as different colors, given in the legend. From Publication III, images reprinted according to the creative commons license CC BY 4.0.

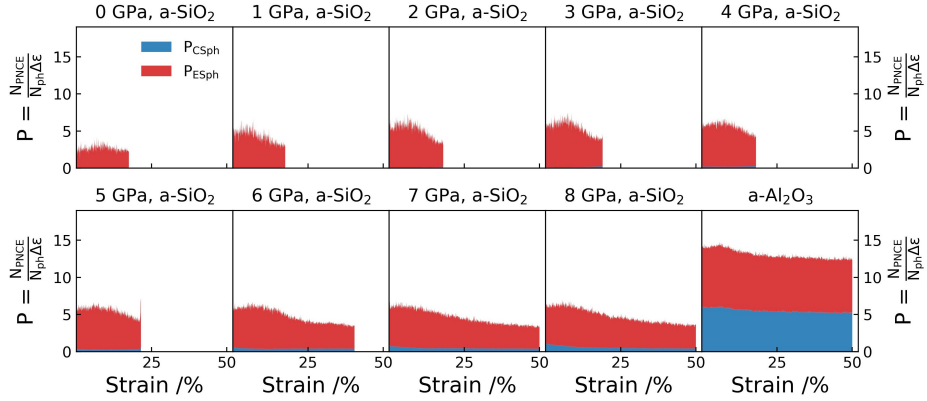


Figure 5.17: Normalized number of events per $\Delta\varepsilon$ strain change for CSph and ESph polyhedra in all structures during stretching, where the x-axis is the engineering strain in percentage, the y-axis indicates how active each type of polyhedron is quantified using Eqs. 4.15 and 4.16. From Publication III, images reprinted according to the creative commons license CC BY 4.0.

neighbor change events than its small number fraction would indicate. In 8 GPa a-SiO_2, with an ESph fraction of 7%, they contribute up to 30% of the PNCEs. Additionally, because an active ESph-CSph pair can also contribute to CSph's activity, CSph is found to be more active when the ESph fraction increases. These factors together result in an increasing plastic deformation ability in the structures that we investigated.

To compare the different activities of CSph and ESph, we normalized the PNCE results according to their corresponding polyhedron type, as presented in Figure 5.17. We can see more clearly that ESph has a much higher neighbor-changing possibility (P) compared to CSph, especially in structures with less plasticity.

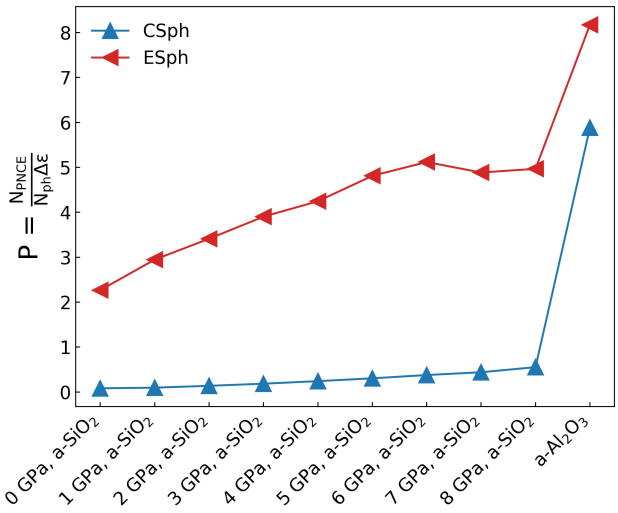


Figure 5.18: Normalized number of events per $\Delta\varepsilon$ strain change for CSph and ESph polyhedra. in all structures at the maximum stress. Y-axis indicates the probability of polyhedral neighbor change events quantified using Eq. 4.15 and 4.16 but only on the 2% strain range around the maximum stress point to compare between structures. X-axis indicates different amorphous structures. From Publication III, images reprinted according to the creative commons license CC BY 4.0.

The P of polyhedra would change with strain, but the variance is not significant. We sliced the P results by 1% before and after the maximum strain and averaged the value of P for each structure to obtain comparable results of P for each structure. The results are presented in Figure 5.18. They quantitatively verify the correlation between the plastic deforming ability of amorphous alumina and its high ESph fraction. We could conclude that plasticity in densified amorphous silica samples possibly correlates with the increase of its ESph fraction. BTD occurs when the ESph fraction is large enough. Moreover, by comparing plasticity in different materials, we show that the coarse-grained analysis can be used as a universal characterization method when investigating the structural properties of oxide glass materials, even multi-element materials.

5.4 Plastic behavior of amorphous gallium oxide

In the last part of our research, we investigated the mechanical properties of amorphous gallium oxide (a-Ga_2O_3) with newly developed machine learning potential. Gallium oxide has phases analogous to alumina and it is also believed that its amorphous state is hard to prepare. With atomistic simulation methods, it is possible to prepare a-Ga_2O_3 with extremely high cooling rates, but the prerequisite is a reliable universal potential. Although potentials have been developed for specific phases of a-Ga_2O_3 [111, 112], the newly developed machine

learning potential has the advantage of describing different phases, as well as the amorphous state [39]. With the help of the potential, we investigated the glass transition and mechanical behavior of a-Ga_2O_3, validate the potential with experimental results, and performed a comprehensive comparison with a-Al_2O_3.

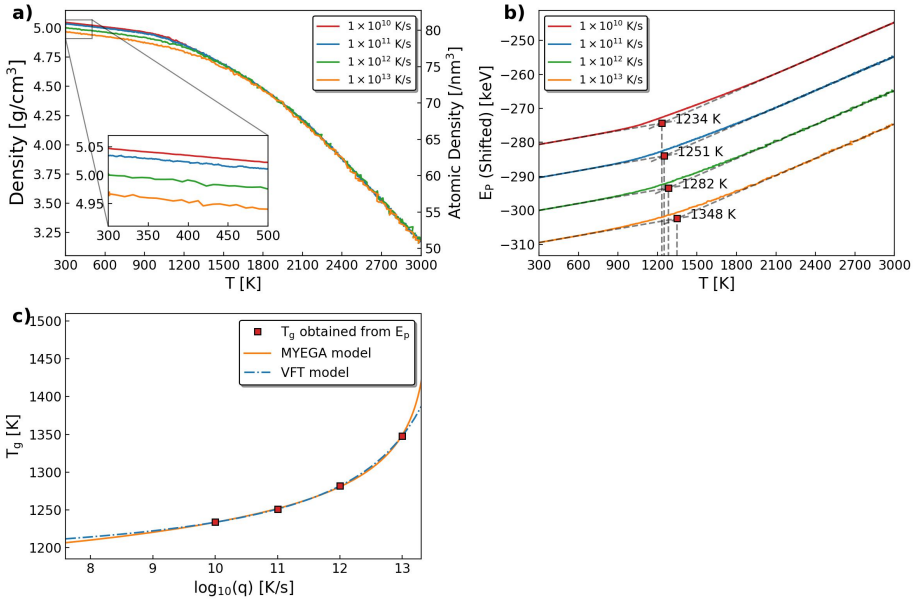


Figure 5.19: (a) The density and atomic density of the Ga_2O_3 structure as a function of temperature, with different cooling rates. (b) Potential energy as a function of temperature during cooling, with different cooling rates. (c) Fit of the T_g data evaluation from potential energy change to the VFT and the MYEGA model. From Publication IV.

Quenching simulations are performed with cooling rates ranging from $1{\times}10^{10}$ to $1{\times}10^{13}$ Ks^{-1}. Unlike the previous settings of a-Al_2O_3, a randomly generated initial structure with 48,000 atoms is used to guarantee the absence of long-range ordering in the first place. The initial structure is equilibrated at 3000 K for 50 ps and cooled down to 300 K afterwards. Figure 5.19(a) presents the mass density and the atomic density as functions of temperature during the quenching process. Without manually adjusting the box size to control the final density, the potential produced a 4% difference in density compared to experimental measurements [37, 112, 113]. Figure 5.19(b) shows the potential energy as a function of temperature, from which we determined the glass transition temperature (T_g) of Ga_2O_3. T_g changes from 1234 K to 1348 K as the cooling rate varies from $1{\times}10^{10}$ to $1{\times}10^{13}$ Ks^{-1}. Different with a-Al_2O_3, no crystallization is observed in a-Ga_2O_3 at $q = 1{\times}10^{10}$ Ks^{-1}.

In Figure 5.19(c) we attempt to fit our T_g data to the VFT model which has been introduced and used in Publication I. And also the MYEGA model [114], which

was proposed much later than the VFT model. It is validated to behave better in 'fragile' glass formers and our fitting intends to compare these two models. For the VFT model, the fitting function is

$$T_g = T_0 - \frac{A}{\log_{10}(Bq)}, \tag{5.5}$$

where A, B, and T_0 are fitting parameters. We obtained A = 305.636 K, B = 1.9679×10^{-15} s/K, T_0 = 1168.87 K. The fitting function of the MYEGA model is

$$\log_{10} q = A - \frac{B}{T_g}\exp(\frac{C}{T_g}), \tag{5.6}$$

where A, B, and C are fitting parameters, and we obtained A = 13.4607 K/s, B = 7.1997×10^{-7} K^2/s, C = 2.7763×10^4 K. Both models produce very good fitting results in the investigated q range. For extrapolation, the MYEGA model shows a surge on T_g at higher q range, and lower T_g at lower q range, compared to the VFT model. Since artificial results has been observed in amorphous silica when quenched at $q = 10^{14}$ Ks^{-1} [98], the prediction of fast detaching from reality of the MYEGA model is possibly reasonable. For the low q part, although crystallization of gallium oxide is not observed in our computational investigation, its strong crystallization tendency possibly indicates that the cooling rate needed for its amorphization is extremely high [39]. This makes verification of the T_g at low q challenging.

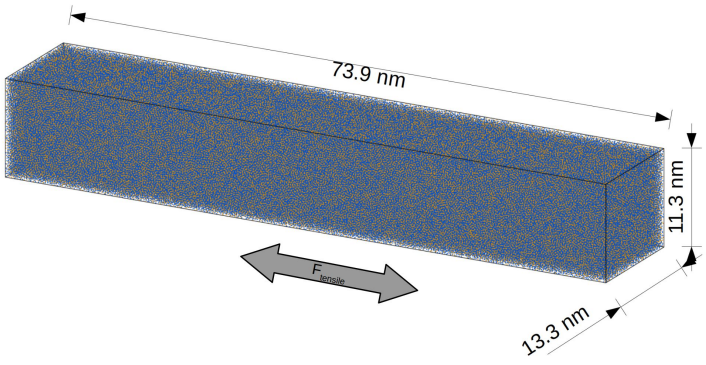


Figure 5.20: Schematic of the simulation box of a-Ga_2O_3 bulk. The arrow indicates the direction of tensile deformation. Ga and O atoms are colored yellow and blue respectively. From Publication IV.

For the mechanical test simulation, we prepared another significantly larger amorphous structure at $q = 1\times10^{12}$ Ks^{-1} to prevent finite-size effects. The excellent computing efficiency of the tabGAP potential makes the use of such a large simulation system feasible. Figure 5.20 shows the amorphous structure before the tension simulations.

The stress and the momentary D^2_{min} as functions of strain can be observed in Figure 5.21(a). Alumina data is included for comparison. Both structures undergo deformation at a strain rate of 5×10^8 s^{-1}. Plasticity can be clearly seen from the stress-strain curves, with a-Ga_2O_3 showing a maximum stress 0.4 GPa lower and a flow stress 0.6 GPa lower than a-Al_2O_3, respectively. By applying the same threshold value for D^2_{min} analysis, it can be seen that these two structures also exhibit closely matching average D^2_{min} values during the tensile tests. According to nanoindentation experiments, the elastic modulus of a-Ga_2O_3 is estimated to range between 100 to 220 GPa [115]. While not entirely comparable, an estimated simulated Young's modulus of 114 GPa for a-Ga_2O_3 can be derived from the initial 1% stress-strain response.

Additionally, we estimated the Poisson ratio (ν) of a-Ga_2O_3 and a-Al_2O_3 from the relative length change correlation along z and y-axis, as depicted in Figure 5.21(b). Data within the first 1% strain is used for the calculation, and ν is calculated as 0.3253 for a-Ga_2O_3, and 0.3215 for a-Al_2O_3. As reported previously [54], from the ν the fragility (m) can be estimated for a glass former with the following equation:

$$m - 17 = 29(\frac{K}{G} - 1), \tag{5.7}$$

where K is the bulk modulus, G is the shear modulus, and m is fragility. Given the correlation between K, G, and ν as

$$\frac{K}{G} = \frac{2}{3}\frac{(1+\nu)}{(1-2\nu)}, \tag{5.8}$$

we can calculate the fragility a-Ga_2O_3 as 61.3328 and for a-Al_2O_3 as 59.5658. It is very likely that a-Al_2O_3 is a 'fragile' glass former [108], consistent with our calculation. Thus the close fragility of a-Ga_2O_3 hints that it may also be a 'fragile' glass former.

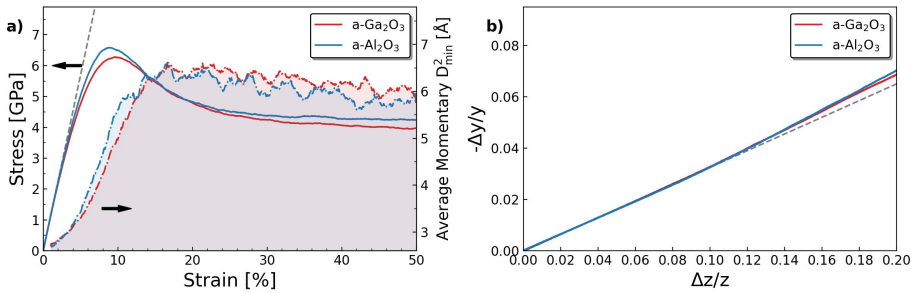


Figure 5.21: (a) Stress and average momentary D^2_{min} as functions of strain during tensile test. Young's modulus was calculated from the linear fitting of the first 1% of the curve. D^2_{min} is calculated with r_{cut} =4.6 Å. (b) Volume change on the dimension orthogonal to the strained dimension as a function of the volume change on the strained dimension in both a-Ga_2O_3 and a-Al_2O_3. Poisson's ratio of a-Ga_2O_3 is fitted from the first 1% strain ($\Delta z/z$ <0.01) data of a-Ga_2O_3. From Publication IV.

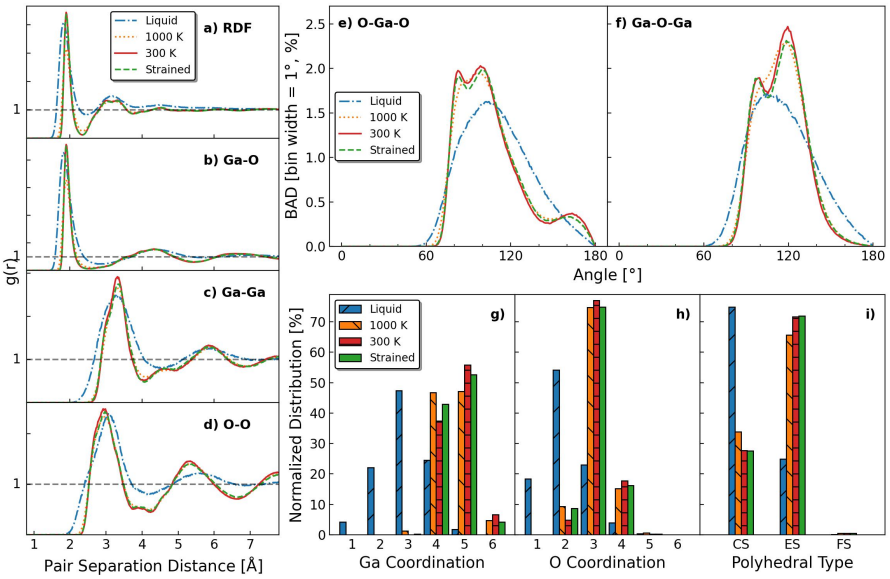


Figure 5.22: (a-d) RDF and PRDFs of the a-Ga_2O_3 structures. (e-f) Bond angle distribution of O-Ga-O and Ga-O-Ga bond angles at 3000 K, 1000 K, 300 K and 50% strained conditions. Cut-off distance is 2.3 Åfor creation of bonds.The bin size is 1° and the results are normalized by the total bond number. (g-i) Coordination distribution of Ga atoms, O atoms, and polyhedra type at 3000 K, 1000 K, 300 K, and 50% strained conditions. The results are normalized by the total number of the corresponding type. From Publication IV.

Before further investigation of the plasticity of a-Ga_2O_3, we first characterized the a-Ga_2O_3 structure to obtain structural information during the quenching and tension, as dipicted in Figure 5.22. RDF and BAD results confirm that the quenched structure shows no long range ordering, indicating that an amorphous state is reached. The RDF results in Figure 5.22(a-d) match well with previous computational results [39, 112]. As a summary, the developed potential shows excellent accuracy and efficiency. We remark that, although using of ML methods does not guarantee higher accuracy of the potential [116], it makes development of interatomic potentials easier. With ML methods, researchers can have interatomic potentials for specifically conditions more easily than before, broaden the usage of classical molecular dynamics methods.

However, direct comparison of amorphous structural infomation should be carefully conducted because subtle differences in the synthesis can result in much more significant differences in the amorphous structure, as discussed in Publication I. This applies for comparison between DFT/AIMD results and classical MD results because of the intrinsic difference on the scale. The coordinate distribution and polyhedral analysis results presented in Figure 5.22(g-i) show that at amorphous state, the 5-fold coordinated Ga and 3-fold coordinated O have the highest fraction, respectively. Polyhedral analysis further reveals that edge-

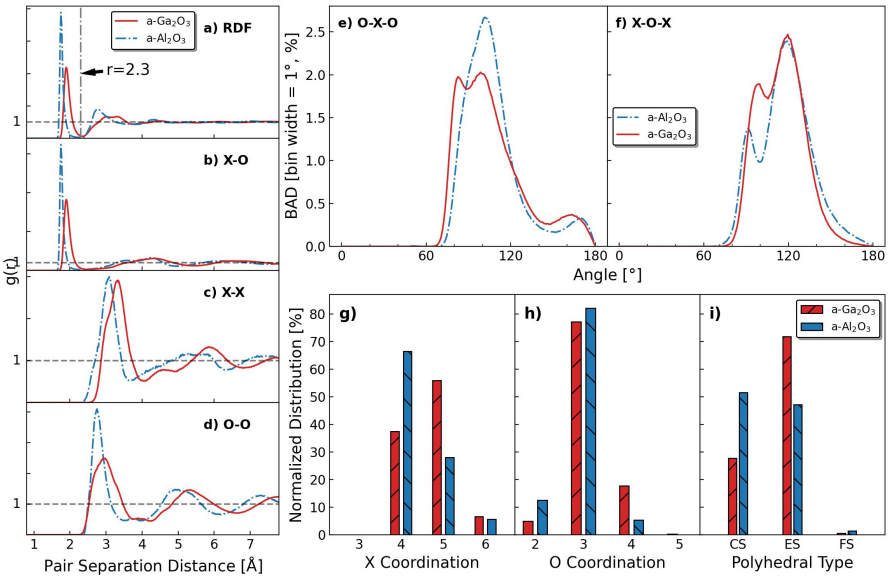


Figure 5.23: (a) RDF and PRDFs of the a-Ga_2O_3 and a-Al_2O_3 structures at 300K. (e-f) Bond angle distribution of a-Ga_2O_3 and a-Al_2O_3 structure. X indicates cation atom Ga or Al. Cut-off distance is 2.3 Å in creation of bonds.The bin size is 1° and the results are normalized by the total number of bonds. (g-i) Coordination distribution of cations, O atoms, and polyhedra type in a-Ga_2O_3 and a-Al_2O_3. Results are normalized by the total number of the corresponding type. From Publication IV.

sharing polyhedra take approximately two-thirds of the total amount. To further compare the plastic deformation ability before a-Ga_2O_3 and a-Al_2O_3, analysis results of the unstrained a-Ga_2O_3 and a-Al_2O_3 structures are compared and shown in Figure 5.23. In general, we see that a-Ga_2O_3 has a comparable or even more closely packed structure than a-Al_2O_3, despite the longer bond length indicated by the RDF. We see that the first peak value for a-Ga_2O_3 is approximately 8% larger than that for a-Al_2O_3. In three dimensions, this can lead to up to 26% difference in atomic density, which explains why there is an atomic density difference between these two materials. Longer bond length may lead to more valid bonds when same cut-off distance is applied in analyzing them, this possibly explains why both coordination distribution and polyhedral analysis results show higher values for a-Ga_2O_3 compared to a-Al_2O_3.

Although the stress-strain curves of a-Ga_2O_3 and a-Al_2O_3 indicate similar plastic deformation ability, we are curious as to how much difference our quantitative characterization can reveal about the plastic deforming ability of these two materials.

From Figure 5.21 we see that the average D^2_{min} values are close to each other in a-Ga_2O_3 and a-Al_2O_3, analyzed at the same r_{cut}=4.6 Å. Subfigures in the first column of Figure 5.24 show the atomic D^2_{min} visualization. We notice possible

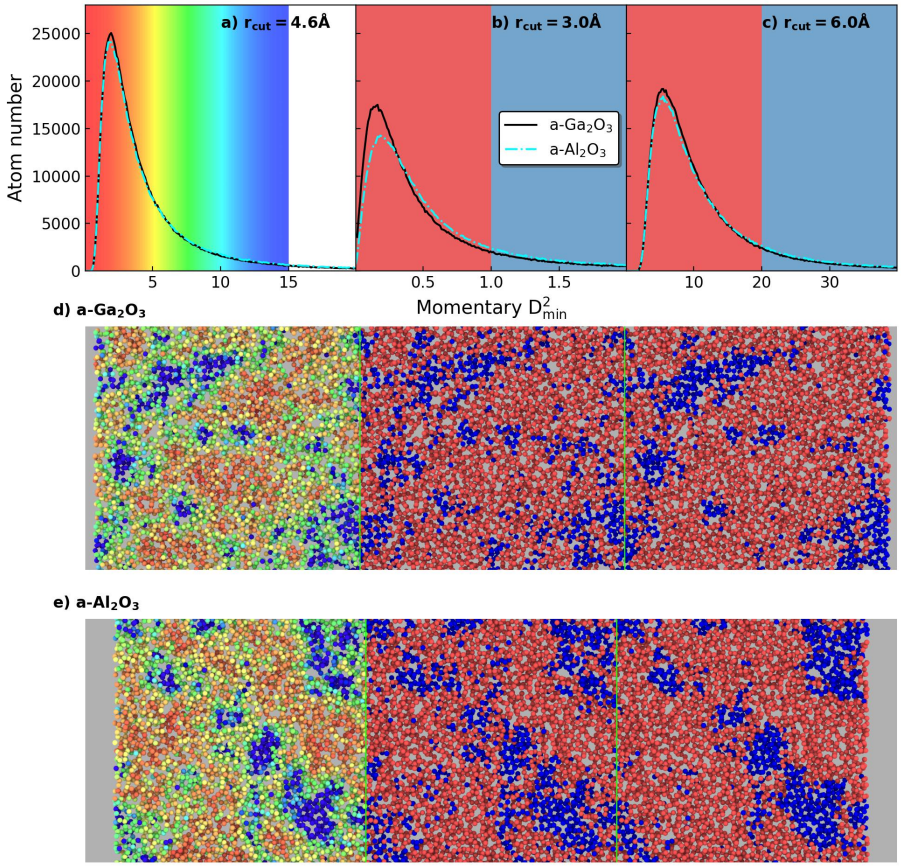


Figure 5.24: Momentary D^2_{min} characterization of a-Ga_2O_3 and a-Al_2O_3 at 50% strain. (a-c) Momentary D^2_{min} distribution calculated using different r_{cut}. Background color indicates the coloring methods. (d-e) Visualization of D^2_{min} calculated using different r_{cut} values. A 5 Å thick slice of a-Ga_2O_3 and a-Al_2O_3 structures are used. Atoms are colored by their momentary D^2_{min} value, as indicated by the background color gradient of (a-c). From Publication IV.

differences in the viscous flow regions from the visualization results. Since the D^2_{min} is sensitive to the r_{cut} value, we wondered whether more information can be obtained by changing r_{cut}. A higher r_{cut} value can include more medium-range structural information, but it could also ignore the localized deformation of small atom clusters. In contrast, small r_{cut} can capture these small strain events, but also bring more noise to the visualization. In Figure 5.24, the atomic D^2_{min} distributions computed with different r_{cut} are shown in the first row. We colored the atom differently with the same threshold value in a-Ga_2O_3 and a-Al_2O_3, as indicated by the background color. Combining the results computed with different r_{cut}, we see that there is an evident difference in the cluster size of high D^2_{min} atom clusters in these two materials. As defined in Ref. [1] and

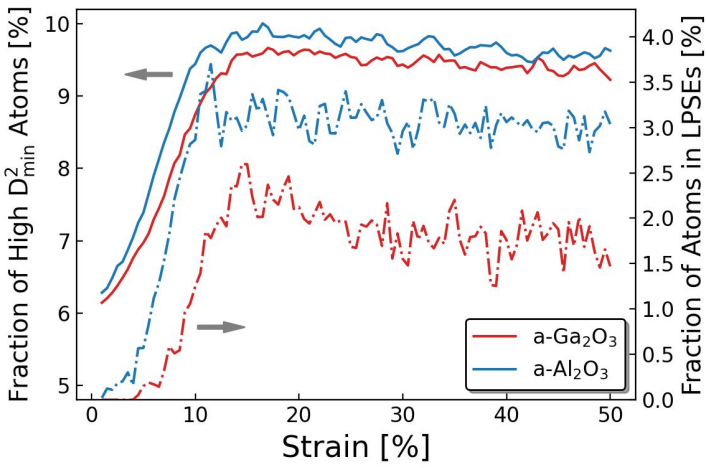


Figure 5.25: The total amount of high D^2_{min} atom fraction (solid lines) and fraction of atoms in LPSEs (dashed lines) as functions of strain during the tensile test. High D^2_{min} atom here means the atoms that have D^2_{min} value higher than two times the average D^2_{min}. An LPSE is defined as a high D^2_{min} atom cluster with more than 200 atoms. From Publication IV.

Publication II, the fraction of atoms in LPSEs as a function of strain is shown in Figure 5.25. It quantitatively shows that despite the similar total fraction of high D^2_{min}atoms, the fraction of atoms in LPSEs in a-Ga_2O_3 is significantly lower than that in a-Al_2O_3. As we found in Publication II, a-Al_2O_3 deformed at different strain rates show comparable high D^2_{min} atom fractions, similar to the case between a-Ga_2O_3 and a-Al_2O_3. Therefore, the results of the tensile test results of a-Ga_2O_3 can be understood as an a-Al_2O_3 structure deformed at a higher strain rate, because there is a lower fraction of atoms in LPSEs. This possibly indicates that during deformation, a-Ga_2O_3 may have a lower LPSE nucleation rate compared to a-Al_2O_3. We predict that at the same strain rate, a-Ga_2O_3 is more likely to plastically deform with a mechanism predominated by shear band slip propagation. However, experimental data is still needed.

Chapter 6

Summary and Outlook

In the thesis, we thoroughly examined the glass transition and plastic deformation abilities of amorphous oxide materials using molecular dynamics techniques.

We began by investigating the glass transition of aluminum oxide and confirmed its occurrence during the quenching process of the molten aluminum oxide. Our findings demonstrate a direct relationship between the cooling rate and the identified glass transition temperature. Subsequent tensile tests were performed and characterized using various analyzing methods. It was observed that the cooling rate has the potential to impact the plasticity of the material by influencing the formation of the structure during the glass transition. By focusing on the structural details in the medium range, disparities in structure can be more effectively identified.

Subsequently, molecular dynamics simulation was utilized to investigate the plastic deformation mechanism of amorphous aluminum oxide. The findings were juxtaposed with experimental data, elucidating at a microscopic scale that the primary mechanism governing plastic deformation in amorphous alumina is mediated by localized plastic strain events (LPSEs). Moreover, based on the characterization results, we concluded that higher strain rates suppress the initiation of LPSEs due to limited time, thereby forcing viscous flow to form near shear bands to mediate deformation. Conversely, lower strain rates permit a more homogeneously distributed nucleation of LPSEs, resulting in a more evenly observed formation of viscous flow within the system.

Following the research conducted on amorphous alumina, our study aimed to broaden our understanding by exploring another commonly used amorphous substance, silica. We conducted computational analysis to investigate the brittle-to-ductile transition under hydrostatic pressure. To address the challenge of comparing the plasticity of different materials, we devised a coarse-grained analytical approach. This method focuses on the polyhedral structural unit comprising a cation and an oxygen atom, providing insights beyond mere short-range ordering.

Based on our findings, we inferred that the presence of an unstable interconnection between polyhedra within the system is the primary factor contributing to increased plasticity in the structure.

In the final section of the study, a recently created machine learning interatomic potential was applied to analyze plasticity in amorphous gallium oxide. It was demonstrated that this potential can accurately generate amorphous configurations that closely match those found in experimental and computational studies. Subsequently, a tensile test was conducted on the generated structure to predict the ability of the material for plastic deformation. The findings of the analysis suggest that amorphous gallium oxide may display plastic properties similar to those of amorphous alumina at ambient temperatures.

In summary, our understanding of amorphous materials, such as glass transition and the mechanism of plastic deformation, has been enhanced through extensive atomistic simulations. Our findings confirm that viscous flow plays a key role in the plastic deformation of the studied amorphous oxide materials. Additionally, we highlight the significance of characterizing the medium-range ordering when studying these types of materials.

In terms of future perspectives, the model established in the thesis offers a fresh approach to quantitatively explore the plasticity in amorphous oxide materials, irrespective of their short-range configuration. Through the suggested characterization method, it becomes feasible to assess the plastic behavior across various amorphous oxide materials or multi-element glasses. The findings outlined in the thesis could potentially enhance the development of robust and long-lasting amorphous materials, paving the way for a new era of ductile ceramics.

Acknowledgements

First, I would like to thank Professor Adam S. Foster and Professor Matti Alatalo for giving me valuable advice as pre-examiners, and thank Professor Morten M. Smedskjær for being my opponent.

The work presented in this thesis has received funding from Academy of Finland research profect PlaCeEra, from the doctoral programme MATRENA. Also, I want to thank the Finnish Grid and Cloud Infrastructure (FGCI), urn:nbn:fi:research-infras-2016072533, and CSC–IT Center for Science, Finland, for provided computational resources.

It has been my fortune to pursuit a PhD at the University of Helsinki. I want to first thank Professor Kai Nordlund for making this possible. His passion and efficiency in scientific research have always inspired me.

I want to thank Professor Flyura Djurabekova. As an international student, she not only gave me guidance in research but also offered immense help in terms of wellbeing. I am very grateful that she could be the custos of my public defense.

I would like to thank Dr., Adj. Prof. Antti Kuronen, who patiently provided guidance from beginning to end. His extensive knowledge and experience in physics and computational science gave me tremendous inspiration. From research to life, he helped me quickly integrate into the team despite the difficult time. You are a great supervisor.

I give my greatest thanks to Dr. Erkka Frankberg for his guidance during my research. Discussion with him was always fruitful and beneficial. His attention to detail was crucial every part of the work in this thesis. I want to also thank colleagues from Tempere University. Thanks to Professor Erkki Levänen for his help during the PlaCeEra project. Thanks to Dr. Janne Kalikka for his help on computational details, discussions with you inspiras me a lot.

I cherish very much the time in Accelerator Laboratory. Big thanks to my dear colleagues, it is always interasting to work with you, talk with you during the coffee break. Althought I was mainly a listener, the time was always enjoyable and helped me to fit in our group quickly. Room D105 was always a warm place, I want to thank Anna, Igor, Jintong, Basil and Christopher. Although not in the room, I would like to especially thank Junlei and Jesper for their assistance with simulations.

Thanks to my family for their constant support. On the road of research, they are my solid backup. And I would like to give my gratitude to Hongyu, thank you for the companion.

At the ending part of this unforgettable journey, I am grateful and excited. The road ahead of me may be long, yet I will search with my will unbending.

Jiahui Zhang

Beijing, 16.6.2024

Bibliography

[1] E. J. Frankberg, J. Kalikka, F. G. Ferré, L. Joly-Pottuz, T. Salminen, J. Hintikka, M. Hokka, S. Koneti, T. Douillard, B. L. Saint, et al., Science **366**, 864 (2019), ISSN 0036-8075.

[2] E. J. Frankberg, *Plastic Deformation of Amorphous Aluminium Oxide* (2018), ISBN 9789521541025.

[3] K. Nomura, H. Ohta, A. Takagi, T. Kamiya, M. Hirano, and H. Hosono, Nature **432**, 488 (2004), ISSN 0028-0836.

[4] H. Tian, Y. Ma, Z. Li, M. Cheng, S. Ning, E. Han, M. Xu, P.-F. Zhang, K. Zhao, R. Li, et al., Nature **615**, 56 (2023), ISSN 0028-0836.

[5] H. Hosono, J. Kim, Y. Toda, T. Kamiya, and S. Watanabe, Proceedings of the National Academy of Sciences of the United States of America **114**, 233 (2017), ISSN 10916490.

[6] G. Karbasian, M. McConnell, H. George, L. Schneider, M. Filmer, A. Orlov, A. Nazarov, and G. Snider, Applied Sciences **7**, 246 (2017), ISSN 2076-3417.

[7] J. Park, I. You, S. Shin, and U. Jeong, ChemPhysChem **16**, 1155 (2015), ISSN 1439-4235.

[8] Y. Idota, T. Kubota, A. Matsufuji, Y. Maekawa, and T. Miyasaka, Science **276**, 1395 (1997), ISSN 0036-8075.

[9] A. Mavrič, M. Valant, C. Cui, and Z. M. Wang, *Advanced applications of amorphous alumina: From nano to bulk* (2019).

[10] P. K. Gupta, Journal of Non-Crystalline Solids **195**, 158 (1996).

[11] E. D. Zanotto and J. C. Mauro, Journal of Non-Crystalline Solids **471**, 490 (2017), ISSN 00223093.

[12] Wikipedia contributors, *Glass — Wikipedia, the free encyclopedia* (2024).

[13] H. MORIKAWA, S.-I. MIWA, M. MIYAKE, F. MARUMO, and T. SATA, Journal of the American Ceramic Society **65**, 78 (1982), ISSN 0002-7820.

[14] J. Neuefeind and K.-D. Liss, Berichte der Bunsengesellschaft für physikalische Chemie **100**, 1341 (1996), ISSN 00059021.

[15] X. Yuan and A. Cormack, Journal of Non-Crystalline Solids **319**, 31 (2003), ISSN 00223093.

[16] R. Dupree, D. Holland, P. McMillan, and R. Pettifer, Journal of Non-Crystalline Solids **68**, 399 (1984), ISSN 00223093.

[17] J. Du and A. Cormack, Journal of Non-Crystalline Solids **349**, 66 (2004), ISSN 00223093.

[18] A. Pedone, G. Malavasi, M. C. Menziani, U. Segre, and A. N. Cormack, Chemistry of Materials **20**, 4356 (2008), ISSN 08974756.

[19] S. Sundararaman, W.-Y. Ching, and L. Huang, Journal of Non-Crystalline Solids **445-446**, 102 (2016), ISSN 00223093.

[20] S. Urata and Y. Sato, Journal of Chemical Physics **147** (2017), ISSN 00219606.

[21] W. Gonçalves, J. Morthomas, P. Chantrenne, M. Perez, G. Foray, and C. L. Martin, Acta Materialia **145**, 165 (2018), ISSN 13596454.

[22] K. Lee, Y. Yang, L. Ding, B. Ziebarth, M. J. Davis, and J. C. Mauro, Journal of the American Ceramic Society **103**, 4295 (2020), ISSN 0002-7820.

[23] Y. Onodera, S. Kohara, P. S. Salmon, A. Hirata, N. Nishiyama, S. Kitani, A. Zeidler, M. Shiga, A. Masuno, H. Inoue, et al., NPG Asia Materials **12** (2020), ISSN 18844057.

[24] Y. Shi, J. Luo, F. Yuan, and L. Huang, Journal of Applied Physics **115** (2014), ISSN 0021-8979.

[25] F. Yuan and L. Huang, Scientific Reports **4**, 5035 (2014), ISSN 2045-2322.

[26] R. Ramachandramoorthy, J. Schwiedrzik, L. Petho, C. Guerra-Nunez, D. Frey, J. M. Breguet, and J. Michler, Nano Letters **19**, 2350 (2019), ISSN 15306992.

[27] Y.-C. Chen, Z. Lu, K. ichi Nomura, W. Wang, R. K. Kalia, A. Nakano, and P. Vashishta, Physical Review Letters **99**, 155506 (2007), ISSN 0031-9007.

[28] J. M. D. Lane, Physical Review E **92**, 012320 (2015), ISSN 1539-3755.

[29] F. Ebrahem, F. Bamer, and B. Markert, Computational Materials Science **149**, 162 (2018), ISSN 09270256.

[30] Z. Zhang, S. Ispas, and W. Kob, Acta Materialia **231**, 117855 (2022), ISSN 13596454.

[31] A. Zeidler, K. Wezka, R. F. Rowlands, D. A. Whittaker, P. S. Salmon, A. Polidori, J. W. Drewitt, S. Klotz, H. E. Fischer, M. C. Wilding, et al., Physical Review Letters **113**, 1 (2014), ISSN 10797114.

[32] M. Murakami, S. Kohara, N. Kitamura, J. Akola, H. Inoue, A. Hirata, Y. Hiraoka, Y. Onodera, I. Obayashi, J. Kalikka, et al., Physical Review B **99**, 1 (2019), ISSN 24699969.

[33] K. Vollmayr, W. Kob, and K. Binder, Physical Review B **54**, 15808 (1996), ISSN 0163-1829.

[34] X. Bidault, S. Chaussedent, W. Blanc, and D. R. Neuville, Journal of Non-Crystalline Solids **433**, 38 (2016), ISSN 00223093.

[35] V. G. HILL, R. ROY, and E. F. OSBORN, Journal of the American Ceramic Society **35**, 135 (1952), ISSN 0002-7820.

[36] T. Wang, W. Li, C. Ni, and A. Janotti, Physical Review Applied **10**, 011003 (2018), ISSN 2331-7019.

[37] Z. Han, H. Liang, W. Huo, X. Zhu, X. Du, and Z. Mei, Advanced Optical Materials **8** (2020), ISSN 2195-1071.

[38] S. Mu and C. G. V. de Walle, Physical Review Materials **6**, 104601 (2022), ISSN 2475-9953.

[39] J. Zhao, J. Byggmästar, H. He, K. Nordlund, F. Djurabekova, and M. Hua, npj Computational Materials **9**, 159 (2023), ISSN 2057-3960.

[40] Y. Zhu, Y. He, S. Jiang, L. Zhu, C. Chen, and Q. Wan, Journal of Semiconductors **42**, 031101 (2021), ISSN 1674-4926.

[41] J. E. Medvedeva, D. B. Buchholz, and R. P. Chang, *Recent advances in understanding the structure and properties of amorphous oxide semiconductors* (2017).

[42] K. Nomura, H. Ohta, K. Ueda, T. Kamiya, M. Hirano, and H. Hosono, Science **300**, 1269 (2003), ISSN 0036-8075.

[43] W. KLEMENT, R. H. WILLENS, and P. DUWEZ, Nature **187**, 869 (1960), ISSN 0028-0836.

[44] A. L. Greer, Science **267**, 1947 (1995), ISSN 0036-8075, 1095-9203.

[45] A. L. Greer and E. Ma, MRS Bulletin **32**, 611 (2007), ISSN 0883-7694, 1938-1425.

[46] W. H. Zachariasen, Journal of the American Chemical Society **54**, 3841 (1932), ISSN 0002-7863.

[47] J. Miao, P. Ercius, and S. J. Billinge, *Atomic electron tomography: 3d structures without crystals* (2016).

[48] Y. Yang, J. Zhou, F. Zhu, Y. Yuan, D. J. Chang, D. S. Kim, M. Pham, A. Rana, X. Tian, Y. Yao, et al., Nature **592**, 60 (2021), ISSN 14764687.

[49] J. Schroers, Physics Today **66**, 32 (2013), ISSN 00319228.

[50] N. Amigo, P. Cortés, and F. J. Valencia, SN Applied Sciences **4**, 281 (2022), ISSN 2523-3963.

[51] P. Jenniskens and D. F. Blake, Science **265**, 753 (1994), ISSN 0036-8075.

[52] A. Nicolas, E. E. Ferrero, K. Martens, and J.-L. Barrat, Reviews of Modern Physics **90**, 045006 (2018), ISSN 0034-6861, 1539-0756.

[53] C. Angell, Journal of Physics and Chemistry of Solids **49**, 863 (1988), ISSN 00223697.

[54] V. N. Novikov and A. P. Sokolov, Nature **431**, 961 (2004), ISSN 0028-0836, 1476-4687.

[55] C. A. Angell, K. L. Ngai, G. B. McKenna, P. F. McMillan, and S. W. Martin, Journal of Applied Physics **88**, 3113 (2000), ISSN 00218979.

[56] W. Kauzmann, Chemical Reviews **43**, 219 (1948), ISSN 0009-2665.

[57] H. Mehrer, *Diffusion in Solids*, vol. 155 (Springer Berlin Heidelberg, 2007), ISBN 978-3-540-71486-6.

[58] R. Brüning and K. Samwer, Physical Review B **46**, 11318 (1992), ISSN 0163-1829.

[59] C. T. Moynihan, A. J. Easteal, J. Wilder, and J. Tucker, The Journal of Physical Chemistry **78**, 2673 (1974), ISSN 0022-3654.

[60] K. Prasai, R. Bassiri, H. P. Cheng, and M. M. Fejer, APL Materials **11** (2023), ISSN 2166532X.

[61] W. Callister and D. Rethwisch, *Material Science and Engineering – An Introduction* (2007).

[62] A. A. Griffith, Philosophical Transactions of the Royal Society of London. Series A, Containing Papers of a Mathematical or Physical Character **221**, 163 (1921), ISSN 0264-3952.

[63] C. B. Carter and M. G. Norton, *Ceramic Materials* (Springer New York, 2013), ISBN 978-1-4614-3522-8.

[64] X. Hu, N. Liu, V. Jambur, S. Attarian, R. Su, H. Zhang, J. Xi, H. Luo, J. Perepezko, and I. Szlufarska, Nature Materials **22**, 1071 (2023), ISSN 1476-1122.

[65] C. Herring, Journal of Applied Physics **21**, 437 (1950), ISSN 0021-8979.

[66] M. W. Barsoum, *Fundamentals of Ceramics* (CRC Press, 2019), ISBN 9781498708166.

[67] Z. F. Zhang, J. Eckert, and L. Schultz, Acta Materialia **51**, 1167 (2003), ISSN 13596454.

[68] R. Narasimhan, P. Tandaiya, I. Singh, R. L. Narayan, and U. Ramamurty, International Journal of Fracture **191**, 53 (2015), ISSN 15732673.

[69] Y. Zhang, L. Huang, and Y. Shi, Acta Materialia **215**, 117016 (2021), ISSN 13596454.

[70] Y. Guo, S. Feng, J. Fu, Y. Yang, R. Zheng, H. Wang, and J. Li, Ceramics International **49**, 9298 (2023), ISSN 02728842.

[71] G. A. Rosales-Sosa, A. Masuno, Y. Higo, and H. Inoue, Scientific Reports **6**, 23620 (2016), ISSN 2045-2322.

[72] M. N. Rahaman, *Ceramic Processing, Second Edition* (CRC Press, 2017), ISBN 9781315157160.

[73] K. Lu, Nanoparticulate Materials: Synthesis, Characterization, and Processing (2012).

[74] F. G. Ferré, E. Bertarelli, A. Chiodoni, D. Carnelli, D. Gastaldi, P. Vena, M. G. Beghi, and F. D. Fonzo, Acta Materialia **61**, 2662 (2013), ISSN 13596454.

[75] T. Salminen, *Production of Nanomaterials by Pulsed Laser Ablation* (2013).

[76] D. Frenkel and B. Smit, *Understanding Molecular Simulation* (Elsevier, 2002), ISBN 9780122673511.

[77] M. P. Allen and D. J. Tildesley, *Computer Simulation of Liquids* (Oxford University PressOxford, 2017), ISBN 0198803192.

[78] J. Du and A. N. Cormack, *Atomistic Simulations of Glasses* (Wiley, 2022), ISBN 9781118939062.

[79] C. W. Gear, Calcolo **25**, 1 (1988), ISSN 0008-0624.

[80] A. P. Thompson, H. M. Aktulga, R. Berger, D. S. Bolintineanu, W. M. Brown, P. S. Crozier, P. J. in 't Veld, A. Kohlmeyer, S. G. Moore, T. D. Nguyen, et al., Computer Physics Communications **271**, 108171 (2022).

[81] H. J. C. Berendsen, J. P. M. Postma, W. F. van Gunsteren, A. DiNola, and J. R. Haak, The Journal of Chemical Physics **81**, 3684 (1984), ISSN 0021-9606.

[82] T. Schneider and E. Stoll, Physical Review B **17**, 1302 (1978), ISSN 0163-1829.

[83] W. G. Hoover, Physical Review A **31**, 1695 (1985), ISSN 0556-2791.

[84] H. Kolsky, Proceedings of the Physical Society. Section B **62**, 676 (1949), ISSN 0370-1301.

[85] G. C. Soares, M. Patnamsetty, P. Peura, and M. Hokka, Journal of Dynamic Behavior of Materials **5**, 320 (2019), ISSN 21997454.

[86] A. Bragov, L. Igumnov, A. Konstantinov, A. Lomunov, and E. Rusin, Journal of Dynamic Behavior of Materials **5**, 309 (2019), ISSN 21997454.

[87] M. Matsui, Mineralogical Magazine **58A**, 571 (1994), ISSN 0026-461X.

[88] B. W. H. van Beest, G. J. Kramer, and R. A. van Santen, Physical Review Letters **64**, 1955 (1990), ISSN 0031-9007.

[89] J. F. Ziegler, J. P. Biersack, and U. Littmark, *stopping and range of ions in solids* (1985).

[90] R. Hockney and J. Eastwood, *Computer Simulation Using Particles* (CRC Press, 2021), ISBN 9780367806934.

[91] E. Pollock and J. Glosli, Computer Physics Communications **95**, 93 (1996), ISSN 0010-4655.

[92] O. T. Unke, S. Chmiela, H. E. Sauceda, M. Gastegger, I. Poltavsky, K. T. Schütt, A. Tkatchenko, and K.-R. Müller, Chemical Reviews **121**, 10142 (2021), ISSN 0009-2665.

[93] A. D. Becke, Journal of Chemical Physics **140** (2014), ISSN 00219606.

[94] J. Byggmästar, K. Nordlund, and F. Djurabekova, Physical Review B **104** (2021), ISSN 24699969.

[95] J. Byggmästar, K. Nordlund, and F. Djurabekova, Physical Review Materials **6** (2022), ISSN 24759953.

[96] J. Byggmästar, A. Hamedani, K. Nordlund, and F. Djurabekova, Physical Review B **100** (2019), ISSN 24699969.

[97] J. Byggmästar, K. Nordlund, and F. Djurabekova, Physical Review Materials **4** (2020), ISSN 24759953.

[98] F. Yuan and L. Huang, Journal of Non-Crystalline Solids **358**, 3481 (2012), ISSN 00223093.

[99] F. Yuan and L. Huang, Applied Physics Letters **103**, 201905 (2013), ISSN 0003-6951.

[100] Z. Zhang, S. Ispas, and W. Kob, Journal of Non-Crystalline Solids **532** (2020), ISSN 00223093.

[101] A. Stukowski, Modelling and Simulation in Materials Science and Engineering **18** (2010), ISSN 0965-0393.

[102] M. L. Falk and J. S. Langer, Physical Review E **57**, 7192 (1998), ISSN 1063-651X.

[103] Jiahui Zhang, *Polikit — a polyhedral analysis tool* (2024), URL `https://bitbucket.org/jiahuijiahui/polikit/`.

[104] X. Yuan and A. N. Cormack, Computational Materials Science **24**, 343 (2002), ISSN 09270256.

[105] H. Vogel, Physikalische Zeitschrift **22**, 645 (1921).

[106] G. S. Fulcher, Journal of the American Ceramic Society **8**, 339 (1925), ISSN 0002-7820, 1551-2916.

[107] G. Tammann and W. Hesse, Zeitschrift für anorganische und allgemeine Chemie **156**, 245 (1926), ISSN 0863-1786.

[108] M. C. Wilding, C. J. Benmore, and J. K. Weber, Journal of Physical Chemistry B **114**, 5742 (2010), ISSN 15205207.

[109] H. Hashimoto, Y. Onodera, S. Tahara, S. Kohara, K. Yazawa, H. Segawa, M. Murakami, and K. Ohara, Scientific Reports **12**, 1 (2022), ISSN 2045-2322.

[110] G. Gutiérrez and B. Johansson, Physical Review B **65**, 104202 (2002), ISSN 0163-1829.

[111] Y. B. Liu, J. Y. Yang, G. M. Xin, L. H. Liu, G. Csányi, and B. Y. Cao, Journal of Chemical Physics **153** (2020), ISSN 10897690.

[112] Y. Liu, H. Liang, L. Yang, G. Yang, H. Yang, S. Song, Z. Mei, G. Csányi, and B. Cao, Advanced Materials p. 2210873 (2023).

[113] Z. Yu, C. D. Overgaard, R. Droopad, M. Passlack, and J. K. Abrokwah, Applied Physics Letters **82**, 2978 (2003), ISSN 00036951.

[114] J. C. Mauro, Y. Yue, A. J. Ellison, P. K. Gupta, and D. C. Allan, Proceedings of the National Academy of Sciences **106**, 19780 (2009), ISSN 0027-8424.

[115] A. K. Battu and C. V. Ramana, Advanced Engineering Materials **20**, 1701033 (2018).

[116] S. Gramatte, V. Turlo, and O. Politano, Modelling and Simulation in Materials Science and Engineering **32** (2024), ISSN 1361651X.